THESIS

CHARACTERIZATION OF FEMTOSECOND FILAMENTS IN AIR

Submitted by

Seth William Wilson

Department of Mechanical Engineering

In partial fulfillment of the requirements

For the Degree of Master of Science

Colorado State University

Fort Collins, Colorado

Spring 2025

Master's Committee:

Advisor: Ciprian Dumitrache
Co-Advisor: Azer Yalin

Alan Van Orden

ABSTRACT

CHARACTERIZATION OF FEMTOSECOND FILAMENTS IN AIR

Laser-induced plasmas (LIPs) offer a promising alternative to conventional ignition methods in high-performance engines, addressing inherent limitations of traditional approaches. Firstly, LIPs can be precisely located within the combustion chamber, enabling ignition in regions with a homogeneously mixed air-fuel ratio. Secondly, LIPs eliminate the need for solid electrodes that act as heat sinks and suffer from erosion in high-pressure environments. Finally, LIPs can achieve combustion with mixtures of lower air-fuel ratios than what is possible via conventional ignition, leading to an increase in fuel efficiency. Consequently, laser-based ignition systems are well-suited for engines with pressures and environments beyond the operating range of conventional spark plugs.

In a nominal nanosecond laser ignition method, a high-power laser is focused down to a point until it reaches an intensity level high enough to begin to breakdown the gas molecules in which it is being focused. Whilst the study of nanosecond laser-induced plasma has been investigated thoroughly, this work aims to provide justification for the use of femtosecond lasers as a “foundational” pulse to prepare the combustion area through pre-ionization. Using femtosecond (fs) lasers for ignition purposes is supported by the large body of research which has investigated the formation of plasma filaments through the self-focusing effect that occurs when a laser exceeds a critical power. The length of these filaments has been shown to be on the order of meters under certain conditions and provide exciting promise in the fields of remote sensing, weather control, and waveguides.

This work obtains information about the filament through the use of optical emission spectroscopy and finds that the lifetime of femtosecond filaments are on the order of nanoseconds whist studied nanosecond plasmas last in excess of tens of microseconds. The spectral emission from the filament is dominated by the N_2(C-B) and N_2^+(B-X). These transitions are observed in nanosecond plasmas, but only at times of greater than 1 μs after the pulse. Femtosecond filaments produce these species almost immediately and their lifetimes are only a few nanoseconds. Using a radiative emission and absorption code, we were able to determine the gas temperatures of the filament to be 500±100 K.

A zero-dimensional plasma kinetics model was developed to simulate experimental conditions derived from optical emission spectroscopy. It was found that N_2(C) formation comes initially from direct electron excitation up from the ground state of N_2(X) then from the dissociation of N_4^+. N_2(C) is destroyed by quenching via O_2 primarily, N_2 secondarily, and deexcited down to N_2(B) ternately.

This work answers two questions. First, how is the plasma generated by a femtosecond laser different from that of a nanosecond laser? Second, what chemical reactions occur in a femtosecond plasma. Experimental testing found physical and thermochemical differences in the femtosecond plasma versus the extensively studied nanosecond plasma, namely the shape, lifetime, emissive properties, and temperature. Theoretical modeling unveiled the reaction pathways responsible for the dominant emissive species found spectrally. Concurrency was found between experimental and theoretical results for the reaction pathway of the dominant emissive species in femtosecond plasmas. This concurrence provides confidence to the reaction pathways presented and opens the door to further research using the knowledge of those reaction pathways to increase the viability of femtosecond laser filaments in combustion applications.

ACKNOWLEDGEMENTS

I must acknowledge the help that I received on all fronts to complete this work. Firstly, I would like to thank my advisors, Dr. Ciprian Dumitrache and Dr. Azer Yalin, for their unwavering support and dedication to helping me through this project. Through their guidance and direction, I gained the confidence that I needed to face the challenges ahead of me. They provided help when I came to a roadblock and assisted me with tasks that I had not yet gained an understanding of. I also thank Dr. Victorien Blanchard for his advice. While not my official advisor, I thank him for the hands-on work that he provided in the experiments and drafting of research papers. Additionally, I am grateful to the members of both Dr. Dumitrache's and Dr. Yalin's research groups for their support and comradery as I pursued my master's degree. From Dr. Yalin's group, thank you, Evan, Brian, Parneeth, Mitchell, Junaid, Jon, Neylson, and Michael. From Dr. Dumitrache's group, thank you, Kavin, Manav, Riley, Eli, Katie, Mozhdeh, Zachary, Kelsie, Abbie, and Spencer.

I also hope to thank the United States Air Force via Grant FA9550-22-1-0424 for funding the project and allowing me to complete this research.

To say that this work was completed without the support of my family would be completely foley. My loving wife Carina has supported me and provided me with encouraged me when I feel that I cannot continue anymore. All the while putting aside her own needs, which are many as she was pregnant with our twin girls during most of my time in graduate school. She chose to serve me selflessly and be the irreplaceable ally that I needed. I must thank her for hearing me ramble on about things she doesn't understand, all the while smiling at me and listening intently. And while they are not yet here, I need to thank my twin daughters for

interrupting my work with ultrasounds and doctor's visits. Those interruptions came as a reminder that my work is not the most important thing in life. I want them to know that even before I heard them speak, they too gave me strength to continue and pursue hard things. In fatherhood, I hope to give them a fraction of the inspiration that they gave to me.

Lastly, I find it necessary to acknowledge my faith and the role it has had in my perseverance as I complete this thesis. My love for engineering has come from what I believe to be an innate desire to understand the world created around me and the intricate details that My Creator has put into motion for humanity to explore. I believe it to be evident that the natural laws that govern our physical reality are not mere accidents nor circumstances but rather the divine fingerprints of He who put them together for us to enjoy and revel in. I consider it necessary to be obedient to the Word of the Lord, as He states in Colossians 3:23 – 24, to work hard with all my heart in whatever I do, knowing that the full reward for this work will not come until the end of my life.

TABLE OF CONTENTS

LIST OF TABLES

LIST OF FIGURES

CHAPTER 1: INTRODUCTION

1.1 Motivation

Laser-induced plasmas (LIP) offer a useful and novel method of combustion initiation over standard methods of ignition. Offering a potential replacement to spark plug ignition systems, laser-induced plasmas offer advantages that are not possible through conventional means. The absence of an electrode surface inside of the combustion chamber eliminates many problems. Spark plug erosion, a problem that especially plagues large gas engines that operate at higher chamber pressures than car engines, is eliminated with laser-induced plasmas [1]. Studies have also shown that the use of plasma-assisted combustion through the use of lasers, or PAC, opens up new reaction pathways through the electron excitation of nitrogen and oxygen atoms, which modify the fuel oxidation pathways significantly [2]. A growing interest has also been seen in using LIP in high-performance scramjet engines [3]. To provide ignition to engines operating in the supersonic and hypersonic regime, it's necessary to create pockets of subsonic air for combustion. This is often done by introducing bluff bodies into the supersonic flow but has the adverse effect of increasing entropy and potentially unstarting the engine [4]. LIP has been shown to promote the generation of intermediate species in the combustion process inside of a hypersonic flow, even to the point of continuous streams of hydroxyl at certain laser repetition rates [3].

It's been shown that LIP can create a more bespoke approach to combustion in its ability to be positioned anywhere in the combustion chamber through alterations of the focusing parameters and optics used for that laser [5]. A laser's wavelength can be tuned to excite certain transitions that can lead to chain-propagating combustion reactions with less energy deposition than conventional ignition [6]. The cumulative potential of LIP to provide ignition solutions to

engines that allow the ability to operate with lower energy deposition requirements, leaner mixture ratios leading to lower polluting emissions (NOx), and the ability to operate in off-nominal environments prove exciting to the fields of propulsion and aeronautics research.

1.2 State of the Art

1.2.1 Conventional Laser-Induced Plasmas

Conventional laser ignition can be achieved through the tight focusing of a high-powered laser pulse through a lens until the focused power of that pulse exceeds the ionization potential of air or whatever gas mixture one intends to create a plasma in. This is commonly referred to as non-resonant breakdown [7]. In this method of breakdown, a single pulse is governed by two driving mechanisms of plasma formation. Those mechanisms are multiphoton ionization (MPI) and electron avalanche impact (EAI). Through these means, one creates a standing spark in midair that resembles that of a conventional spark plug. While this method of LIP does have the potential to be used as an ignition source for high-performance engines, it has disadvantages. The pulse is governed by MPI and EAI mechanisms, which operate under significantly different timescales. Further, the energy deposition into the air with a single pulse is often generated via a q-switched nanosecond pulse width laser. This type of laser generates local thermal pockets over 10,000 K, which is almost two orders of magnitude above the energy requirement for starting combustion. An alternate approach to generating such plasmas is through the use of overlapping laser pulses from two lasers with various properties [8]. First, a pre-ionization pulse is generated, which creates seed electrons primarily through the mechanism of MPI. A second pulse is fired in short succession after this one that serves to add energy into the system via EAI [9]. Through this dual-pulse energy deposition method, one gains the ability to tailor the properties of the generated plasma. It has been found that lasers that operate in the ultraviolet (UV) range of light increase the probability of the MPI processes occurring. This is due to the lower photon

requirement for photoionization [10]. Further, lasers with short pulse durations, on the order of femtosecond or picosecond have also been found to be suitable in use as a pre-ionization pulse, and the ionization process appears to be proportional to the amount of laser fluence [11].

1.2.2 Femtosecond Laser-Induced Plasmas

Femtosecond laser-induced plasma differs from conventional LIP primarily in two ways. One is how the laser is focused down to create high local intensities, and the second is the operational mode by which a laser of that short of a pulse is operating. Femtosecond filamentation, or self-focusing, is similar to the focusing experienced by a laser directed through a lens but the lens is non-physical and is the result of non-linear optical phenomena [12]. In a situation where the intensity of the laser pulse along the axial direction at its front is Gaussian in shape, that is, high intensity at the center which tapers off towards the edges, it is possible for the local index of refraction to change. When this happens, the velocity of that propagation, which is inversely proportional to the index of refraction, slows down where the intensity is the highest. Thus, the edges of this laser front move faster than its center, which results in a curvature of the front towards the central axis of its propagation. In other words, the laser begins to focus simply as a function of its intensity. This phenomenon is unavoidable given a laser of high enough initial power. For an 800 nm laser propagating through air, the critical power to achieve self-focusing is 3.2 GW [13]. Contrary to initial belief, this self-focusing doesn't contradict the laws of diffraction but showcases an interplay between nonlinear Kerr index refocusing and diffraction. The laws of diffraction refer to how a laser spreads out after it passes through a focal point induced by a lens. In simpler terms, when light passes through a small opening or around an object, it doesn't just continue straight forward but spreads out and this spreading of light, or any other wave, is known as diffraction. The nonlinear Kerr index increases in the presence of

intense light radiation, which in the case of an uneven laser wavefront, will start the process of self-focusing [13].

This oscillating behavior results in long propagation lengths, reaching several kilometers under certain conditions. This propagation is significantly longer than the Rayleigh length, indicating the presence of laser filamentation rather than mere optical breakdown. The prospect of such filamentation is advantageous, especially for laser-guided weapons, as it forms a long, self-perpetuating energy channel that can act as a waveguide. Analogous to providing a toy car with a smooth track for better distance coverage compared to gravel, this approach enables any traversing laser beam to efficiently reach its destination. To this point, modeling work has been completed that highlights the use of femtosecond filaments to this end [14].

1.3 Thesis Outline

This thesis investigates the properties of a femtosecond laser-induced plasma and the chemical kinetics therein. In gaining an understanding of the plasma that is generated by the femtosecond laser, an increased knowledge of how it can be utilized for combustion purposes is obtained. Two main goals are held in the pursuit of increasing the knowledge of femtosecond plasmas: 1) investigating the species emission at various wavelengths from the plasma and determining the local temperatures of the plasma, and 2) understanding the reaction pathways that are occurring in the plasma that generate excited species useful for combustion. The thesis achieves these goals via the combination of experimental data collection and theoretical modeling. As such, the organization of the thesis is placed into five chapters. Chapter 1 draws out the motivation for this work and investigates the current state of conventional laser-induced plasmas and how they differ from femtosecond-induced plasmas. Chapter 2 describes the theory and first principles essential for the work to follow. This chapter serves as a launchpad from which the experimental and modeling work gain their merit. As such, the physics of

filamentation is expanded upon, and the operation of the experimental data collection tools is described. Chapter 3 presents a test campaign that utilizes optical emission spectroscopy to obtain experimental data for emitted wavelengths of light from the plasma and their relative intensity. Further characterization of the femtosecond LIP comes from using a radiative code known as Specair to fit the experimental spectral data. From the fitted spectral data, a determination of the gas temperature is inferred, and time-resolved spectral data show the temperature is steady for the lifetime of the filament. From this, the mechanism of formation for the predominant excited species production is theorized. Chapter 4 expands on this theory through the use of zero-dimensional plasma kinetics modeling to provide a baseline for the species' density and reaction pathways. The validation of the modeling work comes through comparison to the experimental data and other published models. The numerical modeling work provides access to the formation and loss mechanisms for each species in the chemical kinetics pathway. Modeling of the electron number density and electron temperature is encompassed in the model as a function of time. The thesis is concluded in Chapter 5, where a summary of the main findings is presented. The connection between the motivation for the work and how the collected data supports that motivation is explored. The future work that needs to be completed to expand upon what has been done is outlined.

CHAPTER 2: THEORY AND FIRST PRINCIPLES

2.1 Introduction

The purpose of this chapter is to describe the phenomenon of femtosecond laser filamentation through physical and mathematical means. Filamentation has been studied at length in the writings of Shneider [9], Chin [12,15], Couairon [13] and Raizer [16]. Filamentation, in its most basic terms, is the result of the competing effects of self-focusing and plasma generation. Once a pulse exceeds a certain power level, it will begin to collapse in on itself and focus under its own effects. This leads to an increase in intensity. The high levels of intensity lead to ionization, which then forms a low-density plasma, which defocuses the beam. From here, the process is cyclical. To understand filamentation, one must have a background understanding of the mechanisms that are at play in conventional laser-induced plasma, namely multiphoton ionization (MPI) and electron avalanche ionization (EAI).

Multiphoton ionization (MPI) serves as the primary initiator of free electrons within the system of LIP. During MPI, a neutral molecule absorbs multiple photons, gaining sufficient energy to become ionized [17]. This ionization process results in a positively charged molecule and a free electron. This process is shown schematically in Figure 1-a. Once liberated, these free electrons propagate through the medium and gain energy from the electric field via inverse bremsstrahlung absorption of laser radiation.

In inverse Bremsstrahlung absorption, free electrons absorb energy from the laser field during collisions with neutral or ionized particles. Unlike direct absorption, where photons interact directly with electrons, inverse bremsstrahlung involves electron-photon interactions mediated by a third particle, typically an ion or neutral molecule. The free electrons in the presence of a strong laser field absorb or emit photons whilst colliding with heavier molecules.

In this process the momentum is conserved primarily by the heavier molecule. This process enables electrons to gain energy from the laser field, leading to a gradual increase in their kinetic energy. As these energized electrons continue to ionize other molecules, a cascade of secondary ionization events occurs, producing additional free electrons in a process known as electron avalanche ionization (EAI), see Figure 1-b.

This electron avalanche, however, is limited by competing loss mechanisms, preventing indefinite propagation. These loss processes include electron attachment, where free electrons recombine with other molecules, energy loss through inelastic collisions, and diffusion of electrons away from regions of high ionization.

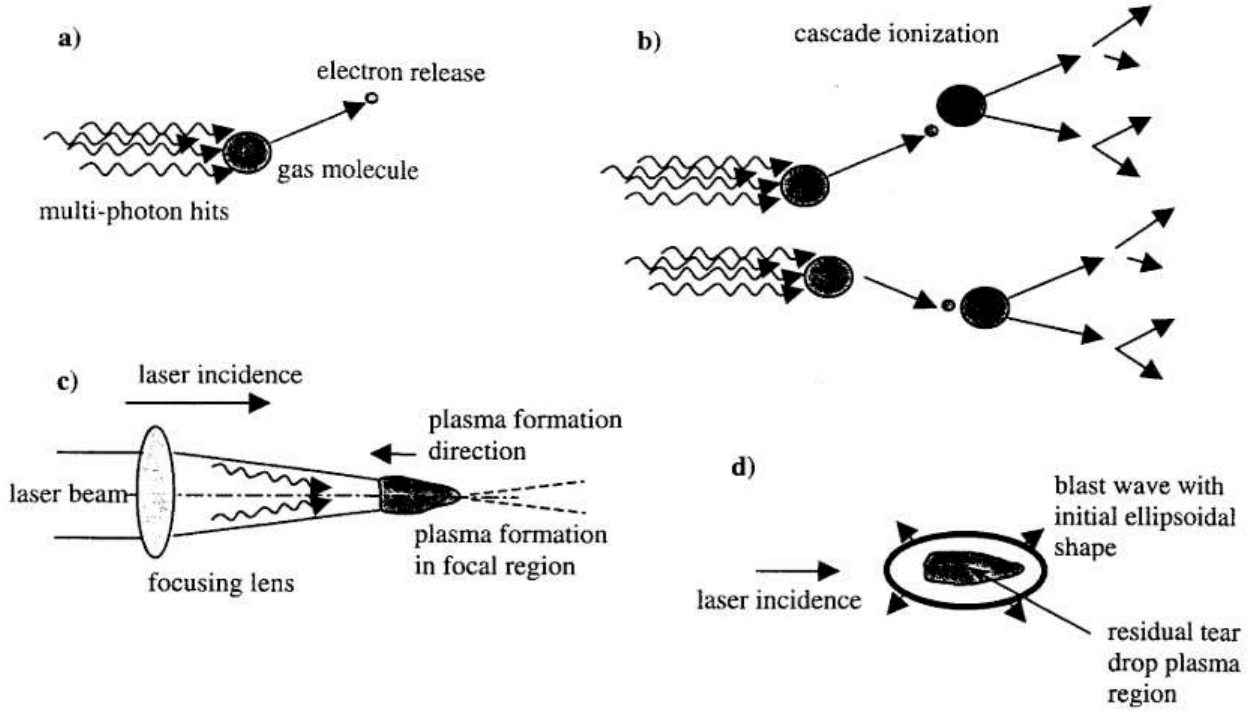

Figure 1. Schematic representation of stages of conventional laser-induced plasma breakdown. (a) Multiphoton ionization, (b) electron avalanche ionization, (c) plasma formation and propagation, (d) plasma shock wave formation [17]

2.2 Femtosecond Filamentation

2.2.1 Self-Focusing

The phenomenon of femtosecond laser filamentation arises from a dynamic interplay of nonlinear focusing and defocusing mechanisms as a high-power laser pulse propagates through a

medium like air. This effect is initiated when the laser's power exceeds the critical power threshold for the medium, resulting in self-focusing due to the nonlinear Kerr effect.

The refractive index of a medium is comprised of two components: the linear refractive index n_0 and the nonlinear component, known as the Kerr index n_2. They are coupled together via the equation: $n = n_0 + n_2 I(r,t)$, where n_0 is the linear index of refraction and $I(r,t)$ is the time and space-dependent value of intensity. The nonlinear component is associated with the third-order susceptibility of the medium, which quantifies the medium's susceptibility to nonlinear optical effects in the presence of high-intensity fields [18]. This susceptibly is given by $\chi^{(3)} = 4\epsilon_0 c n_2 n_0^2/3$ where ϵ_0 is the permittivity of a vacuum and c is the speed of light in a vacuum. The nonlinear Kerr index is usually positive, meaning there is an increase in the index of refraction in the presence of high laser radiation. Thus, given that the velocity of propagation of light through a medium is equal to c/n where c is the speed of light in a vacuum and n is the total index of refraction, light will travel slower through the region where the index of refraction is the highest. This is the same law that governs the focusing of light through a traditional lens. However, in the case of self-focusing the lens is created as a result of the laser itself. This is shown schematically in Figure 2. Self-focusing can overcome the laws of diffraction for a Gaussian-shaped beam when the input power exceeds a critical threshold given by the equation: [19].

$$\mathrm{P_{cr}} \equiv \frac{3.77\lambda^2}{8\pi n_2 n_0} \qquad 2\text{-}1$$

It is therefore shown that the only parameters that self-focusing depends on are the linear and nonlinear index of refraction of the medium, n_2 & n_0, and the wavelength λ. Once the process of self-focusing has started, it will continue, and the local intensity of that spot will increase. Thus,

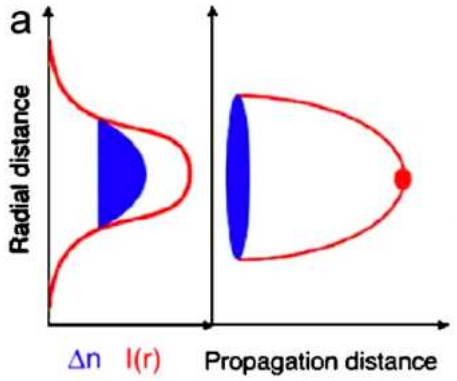

Figure 2. Schematic representation of the nonlinear Kerr index causing self-focusing of a laser beam [13]

the intensity reaches such a high value that ionization begins to occur, free electrons are generated, and plasma formation begins.

2.2.2 Multiphoton Ionization

Earlier, the process of conventional LIP was discussed through the use of four processes. It is important to note that the timescales of these processes are several orders of magnitude apart. The process of MPI takes place in the sub-nanosecond whilst EAI takes place over longer than nanosecond timescales [8]. Further, in the case of femtosecond filaments, the pulse length is shorter than the timescale of a free electron released through MPI, meaning there is no time for that electron to get accelerated from inverse bremsstrahlung absorption, and EAI does not take place at all.

Given this lack of electron acceleration in femtosecond filaments, it becomes essential to quantify the mean free time of a free electron to better understand the dynamics at play. The mean free time of a free electron can be found by the equation [16]

$$(\Delta t)_{mean} = \left(\frac{1}{\sigma N_a \nu_e}\right) \qquad 2\text{-}2$$

where $(\Delta t)_{mean}$ is the mean free time, σ is the collisional cross-section of the electron and neutral molecule, N_a is density, and ν_e the electron velocity. Consider the case of a femtosecond

laser pulse in air. The N_a of air at one atmosphere is 2.68×10^{19} cm^{-3}. In the range of electrons with a kinetic energy of 1 to 6 eV, σ is ~ 10^{-15} cm^2 [16].

In the presence of a laser field, the free electron will gain kinetic energy according to the equation [20]

$$\frac{(e^2E^2)}{(4m\omega^2)}(eV) = (9.33E-14)I(W/cm^2)\lambda^2(\mu m) \qquad 2\text{-}3$$

where e and m are the electron charge and mass, ω is the laser frequency, E the electric field strength induced by the laser pulse, I the pulse intensity, and λ the wavelength. Given that the intensity I of femtosecond laser filaments peaks around 10^{13} W/cm^2, thereby using a range of 10^{13} W/cm^2 to 10^{14} W/cm^2, equation (2-3) evaluates to 0.6 and 6.0 eV [13]. Therefore, knowing that electron velocity v_e is linked to kinetic energy via the equation:

$$\mathrm{KE} = 1/2\mathrm{m_e}\mathrm{v_e^2} \qquad 2\text{-}4$$

v_e is found to be between 4.5×10^7 and 1.4×10^8 cm/s. Thus, the $(\Delta t)_{mean}$ for an electron in the presence of a femtosecond laser pulse is 300-800 fs. From this, it can be seen that the mean free time of an electron generated by MPI via a femtosecond laser will not survive long enough for EAI to occur. Thus the ionization mechanism of femtosecond-induced plasmas is primarily MPI driven.

The generation of plasma invokes a local reduction in the refractive index according to the equation: [21]

$$\mathrm{n} \cong \mathrm{n_0} - \frac{\rho(r,t)}{2\rho_c} \qquad 2\text{-}5$$

where $\rho(r,t)$ is the density of free electrons, in this case generated by MPI, and ρ_c is the critical density of plasma above which it becomes opaque. That value is given by $\rho_c \equiv \epsilon_0 m_e \omega_o^2/e^2$. The density of the generated plasma is highest at the center of the beam, where the intensity is also

the highest. Therefore, from the same point that the laser began to focus from the nonlinear Kerr index, it also defocuses from the generation of plasma. This defocusing is shown in Figure 3.

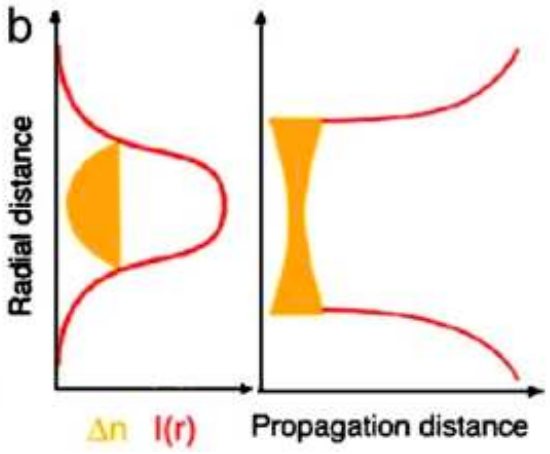

Figure 3. Defocusing of a beam as a result of plasma formation at the center of the beam [13]

Thus, the phenomenon of femtosecond laser filamentation arises from a dynamic interplay of nonlinear focusing and defocusing mechanisms as a high-power laser pulse propagates through a medium like air. This effect is initiated when the laser's power exceeds the critical power threshold for the medium, resulting in self-focusing due to the nonlinear Kerr effect. In this process, the center of the beam travels at a lower phase velocity than its edges, generating a self-focusing effect. The defocusing effect occurs with the creation of plasma. That plasma is generated through multiphoton ionization and creates a force to balance out the Kerr index by increasing the index of refraction. The intensity is highest at this balancing point. In fact, at this point one can observe the condition of intensity clamping [22]. That is to say, the maximum achievable intensity of a Ti:Saphire laser-generated filament is on the order of 4×10^{13} W/cm^2. After this point, the pulse will start to diverge. After a certain distance of divergence, the Kerr index effect will gradually increase as the plasma density decreases, and the process demonstrates a cyclical nature. This is shown schematically in Figure 4. In actuality, a

femtosecond filament has the appearance of a laser bullet suspended in air and is visible to the naked eye. The filament is generated by a Ti-sapphire with a central wavelength of 800 nm through the use of a 750 mm plano convex lens. The filament was produced via a Spectra Physics Solstice Ace laser with a repetition rate of 1 kHz and is approximately 63 mm in air at 1 atmosphere of pressure, as shown in Figure 5.

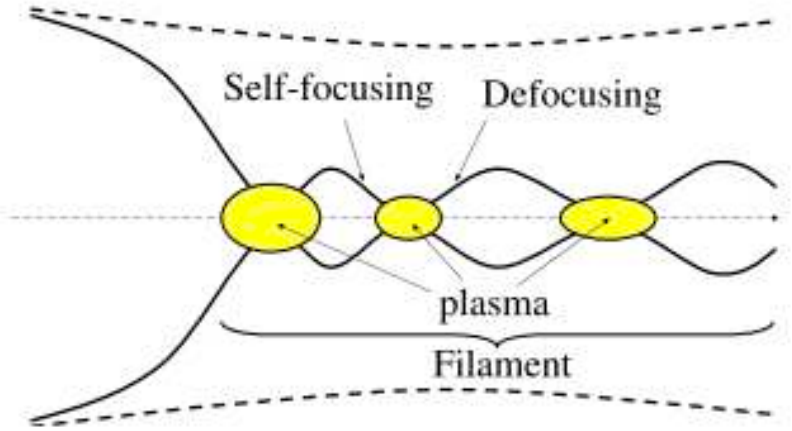

Figure 4. Schematic of the cyclical focusing and defocusing of a filament due to the nonlinear Kerr index and plasma generation [13]

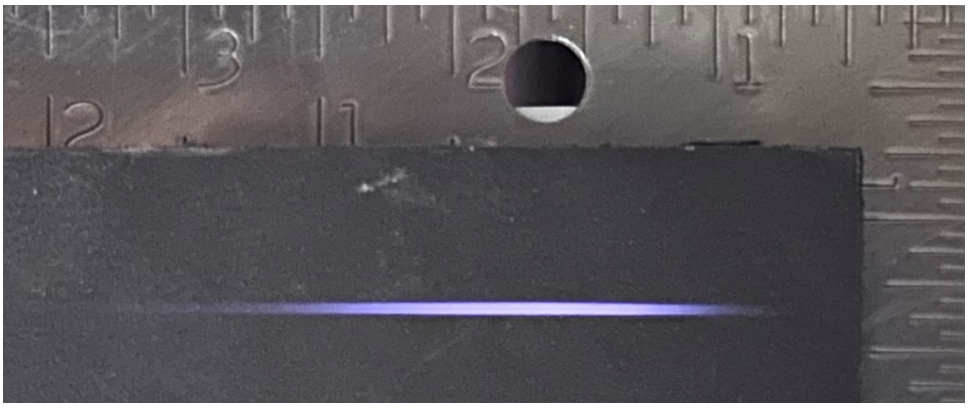

Figure 5. Femtosecond Filament in Air

2.3 Optical Emission Spectroscopy

2.3.1 Energy Level Transitions

Optical Emission Spectroscopy (OES) is a diagnostic method that can discern the intensity of various wavelengths of light. Therefore, it can be used as an analytical technique to

determine the composition and properties of gasses by analyzing the light they emit. This emitted light is referred to as an emission spectrum. When atoms or ions in a material are excited—often through heating, plasma, or laser exposure they emit light at characteristic wavelengths as they return to lower energy states. A basic rendering of this process is shown in Figure 6.a.

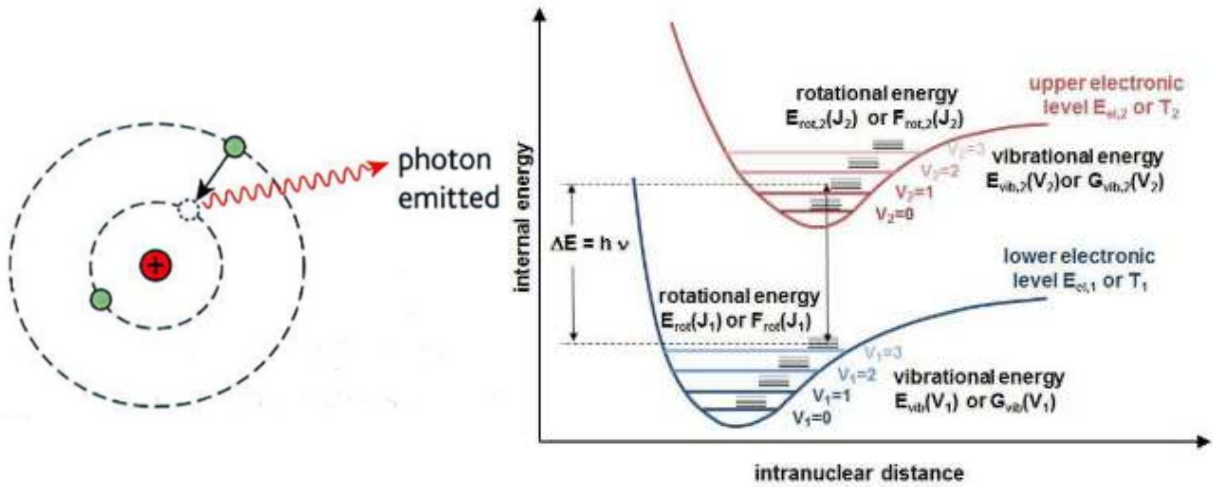

Figure 6. a) A basic rendering of the photon emission process from electron de-excitation. b) Illustration of rotational and vibrational transition levels between two electronic levels [23] [24]

By measuring these wavelengths, OES can identify and quantify the elements present. Consider a molecule in its ground state. It is possible for that molecule to become excited through the absorption of photons incident from a laser pulse. The molecule can become excited to various discrete rotational, vibrational, or electronic levels. The energy difference between the transition from ground state to various excited states can be displayed in an energy level diagram. The differences in the resolution of the various energy level types are shown in Figure 6.b [23].

The molecule will not remain in this excited state E_2 indefinitely but will decay back down to its ground state E_1. When it decays, it will release a photon of equal energy to the transition that just occurred. Thus, the resulting photon's frequency can be determined by

$$\nu = \Delta E/h \qquad 2\text{-}6$$

where h is Planck's constant and $\Delta E = E_2 - E_1$. From this, the associated wavelength of that photon can be determined via

$$\lambda = c/\nu \qquad 2\text{-}7$$

where c is the speed of light in a vacuum and λ is the wavelength of the emitted radiation.

From this, if one were to be able to capture and catalog the emission of photons from a plasma, it's possible to determine which excited species are present in the mixture and at what relative quantities depending on the intensity of each wavelength of light emitted.

2.3.2 Spectrographs and Plasma Spectroscopy

Photons can be captured and observed through the use of a spectrograph. A spectrograph is an optical device that can spread out the wavelengths of light from a source into a spatial axis. This is accomplished through the use of a combination of parabolic mirrors and a diffraction grating. The specific configuration of the spectrograph that was used in the present experiments is a Czerny-Turner spectrograph. A schematic of this configuration is shown in Figure 7. For this style of spectrograph, light enters through the entrance slit and becomes collimated through a parabolic mirror. This collimated light then interacts with a diffraction grating, and the

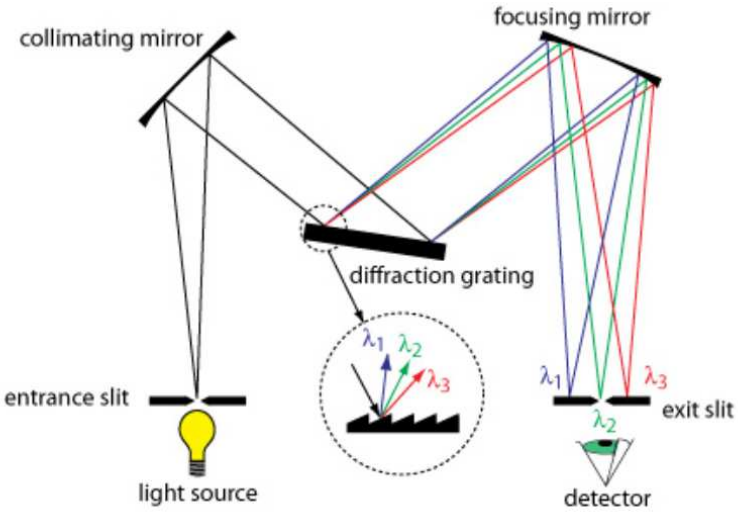

Figure 7. Components of a spectrograph (Czerny-Turner Configuration) [24]

constituent wavelengths of light that compose the collimated light are separated as a function of their reflection off of the diffraction grating [24]. As these constituent wavelengths travel through the device, they are focused down onto the detector but their position along the horizontal axis is now a function of their wavelength. If the diffraction grating were to be placed on a servo motor, one could rotate the grating and allow certain wavelengths of light to exit through the slit and be detected. Thus, a relationship between diffraction grating rotational position and wavelength is generated. After calibration, this device serves as a reliable way to determine which wavelengths of light are interacting with the detector as a function of the diffraction gratings rotational position. A raw experimental image collected by a spectrograph is shown in Figure 8.

In actuality, this is typically not a single-shot image, but the average result of several images stacked on top of one another. This is done to reduce the experimental noise that is present in the system. Further, background subtraction is applied that takes the light from the

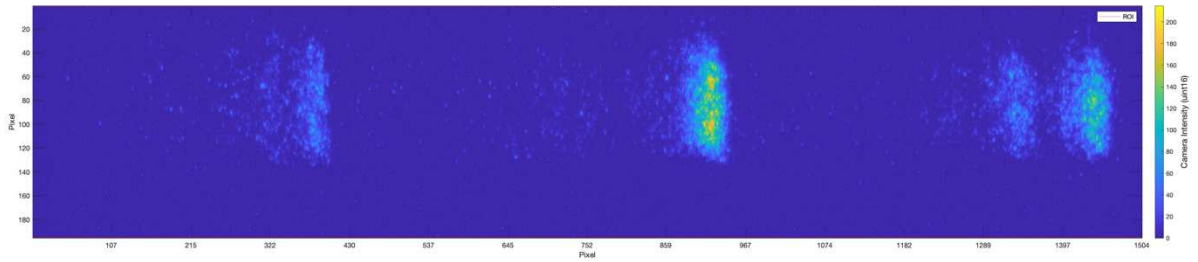

Figure 8. Raw experimental output image from a spectrograph before a conversion to wavelength has been applied

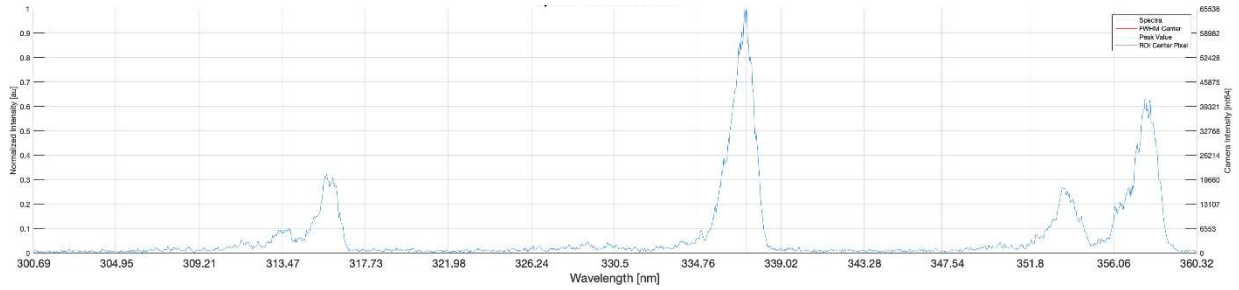

Figure 9. Spectra from the experimental image shown above. Notice the horizontal axis has been converted to wavelength as a function of pixel position. The vertical axis is shown with two scales: the left as a normalized intensity and the right as a pure camera intensity

room and subtracts it from the emitted light to isolate only the subject of interest. This image has not yet been converted to wavelength on the horizontal axis, but it shows the presence of local peaks of light spread along the horizontal direction. From this experimental image, one can construct a spectrum by summing all the values of the pixels in the vertical direction and plotting those values as a function of wavelength. This is shown in Figure 9.

2.4 Specair

After the construction of a spectrum like in Figure 9, to identify the transition emissions that are present in the data, one can use a line-by-line radiative plasma emission code like Specair [25]. Specair computes the plasma emission or absorption spectra based on a quantum mechanical model that describes the energy level transitions of the most important radiating molecules that are present in air plasmas [26]. A subset of those species are N_2, O_2, NO, N_2^+, N, O, and C. Specair can also import experimental spectra and use a fitting algorithm to match the experimental spectra with the sum of various computed spectra. The computed spectra are

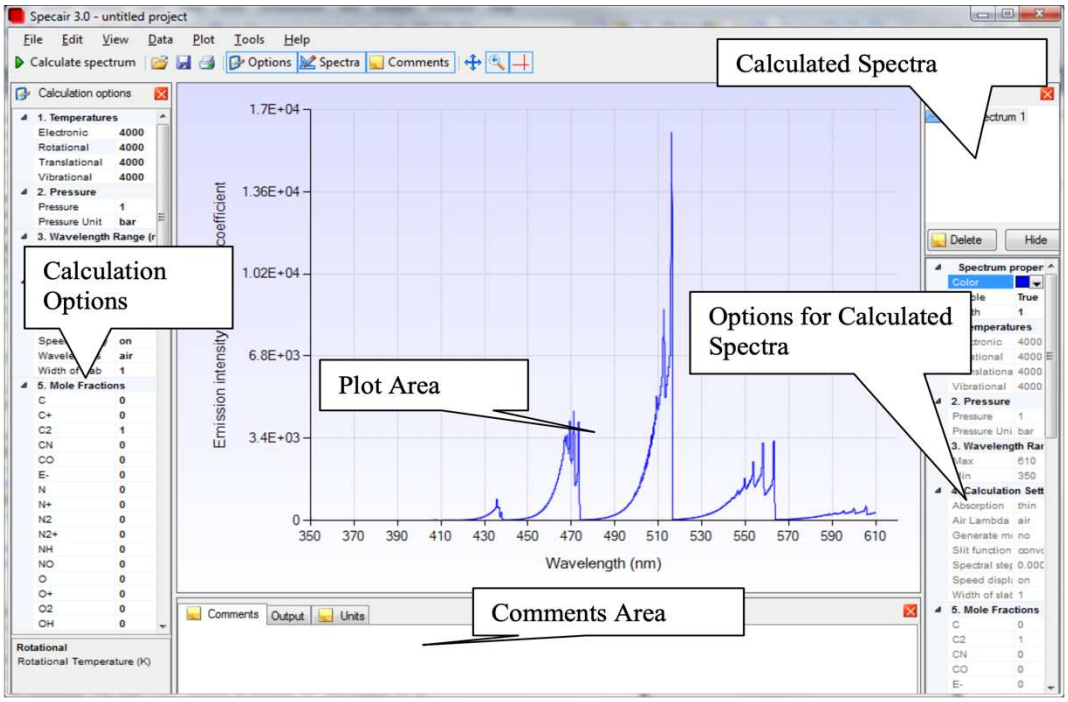

Figure 10. A screenshot from the user interface of Specair [25]

primarily a function of temperatures and mole fractions which are adjusted to reduce the residual between experimental and computed data. In simple terms, Specair solves for the electronic, vibrational, rotational, and transitional temperatures of species and their respective mole fractions in a plasma emission by fitting computed data to experimental data.

2.4.1 Boltzmann Analysis

Boltzmann analysis is a technique used to determine thermodynamic properties, in this case temperature, by analyzing the population distribution of particles among various energy states. The method is based on the Boltzmann distribution, which describes how particles in a system are distributed across energy levels at thermal equilibrium. The ratio of the number of particles in two energy states $\frac{N_i}{N_j}$ is proportional to the negative exponent of the energy of those states, E_i & E_j as given in the equation

$$\frac{N_i}{N_j} = \exp\left(-\frac{E_i - E_j}{k_B T}\right) \qquad 2\text{-}8$$

where k_B& T are the Boltzmann constant and temperature respectively. Knowing that particle transition between energy states leads to the emission of photons with wavelength proportional to the energy difference between states, the relative populations of each energy level can be determined.

The radiative code Specair can cross-reference experimental data with a catalog of known energy level transitions as a function of temperature [25,26].

2.4.2 Fitting Experimental Spectra

The experimental data like that shown in Figure 9 is imported into Specair as a list of wavelengths and corresponding intensity values. These values are then normalized so that the maximum within a given wavelength range equates to a value of 1, and the minimum to 0, with

all proportions kept constant in between. An imported experimental spectra can be seen in Figure 11.

To account for experimental broadening of the spectral lines, an experimental slit function is convoluted unto the experimental spectra. The slit function is collected from a HeNe laser that has a narrow wavelength about 633 nm. The HeNe laser is imaged onto the spectrometer and any broadening that occurs about 633 nm on the data is assumed to be the result of experimental broadening. This broadening is accounted for by Specair when calculating the synthetic spectra used to identify the local transitional peaks and subsequent temperatures. The slit function and the raw image captured by the camera can be seen in Figure 12.

To identify the molecular and atomic species present in our spectral image, we use the Specair Find Transition Tool. This tool automatically finds the molecular transition and corresponding temperature that reduces the residual between synthetic and experimental data. The tool is shown in Figure 13.

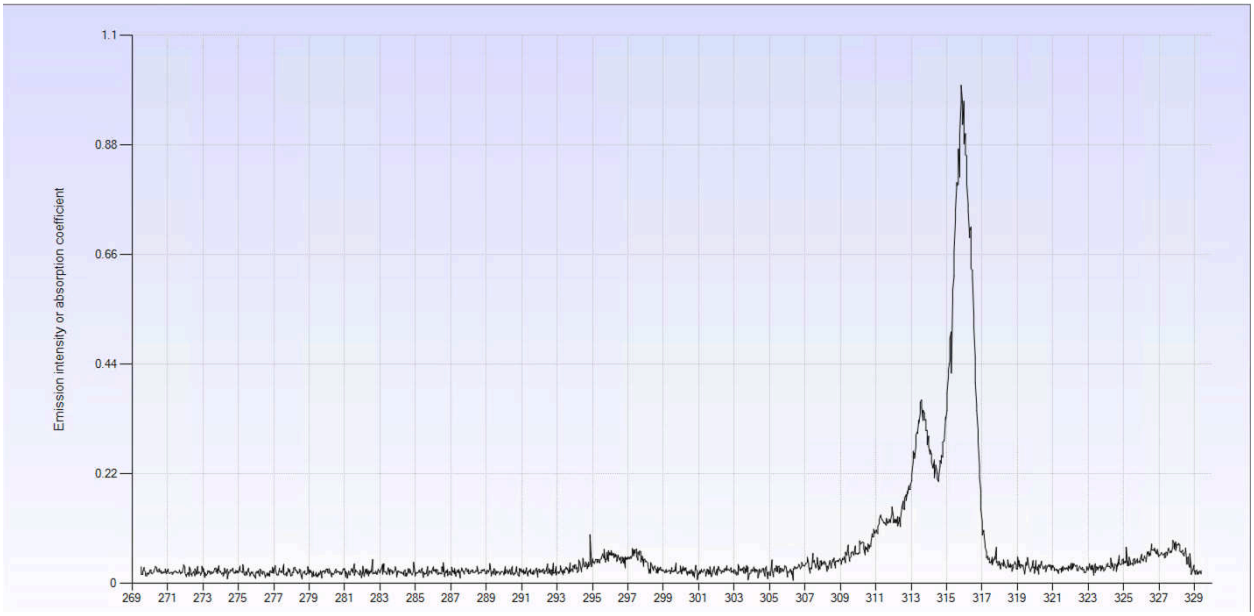

Figure 11. An imported experimental spectrum shown in Specair. The range of intensity values are normalized so that the maximum is 1 and the minimum is 0.

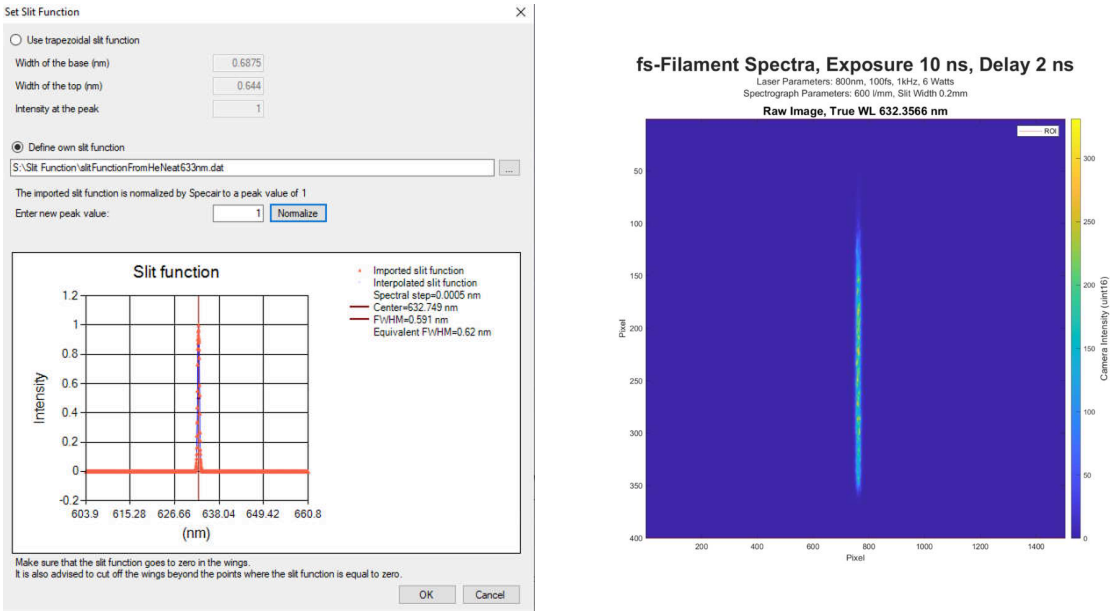

Figure 12. Right: The Slit Function tool within Specair used to define the experimental broadening seen by our hardware. A HeNe laser at 633 nm is imaged and any broadening seen is assumed to be the result of hardware. Left: The raw experimental image from the camera shown the single line at 633 nm.

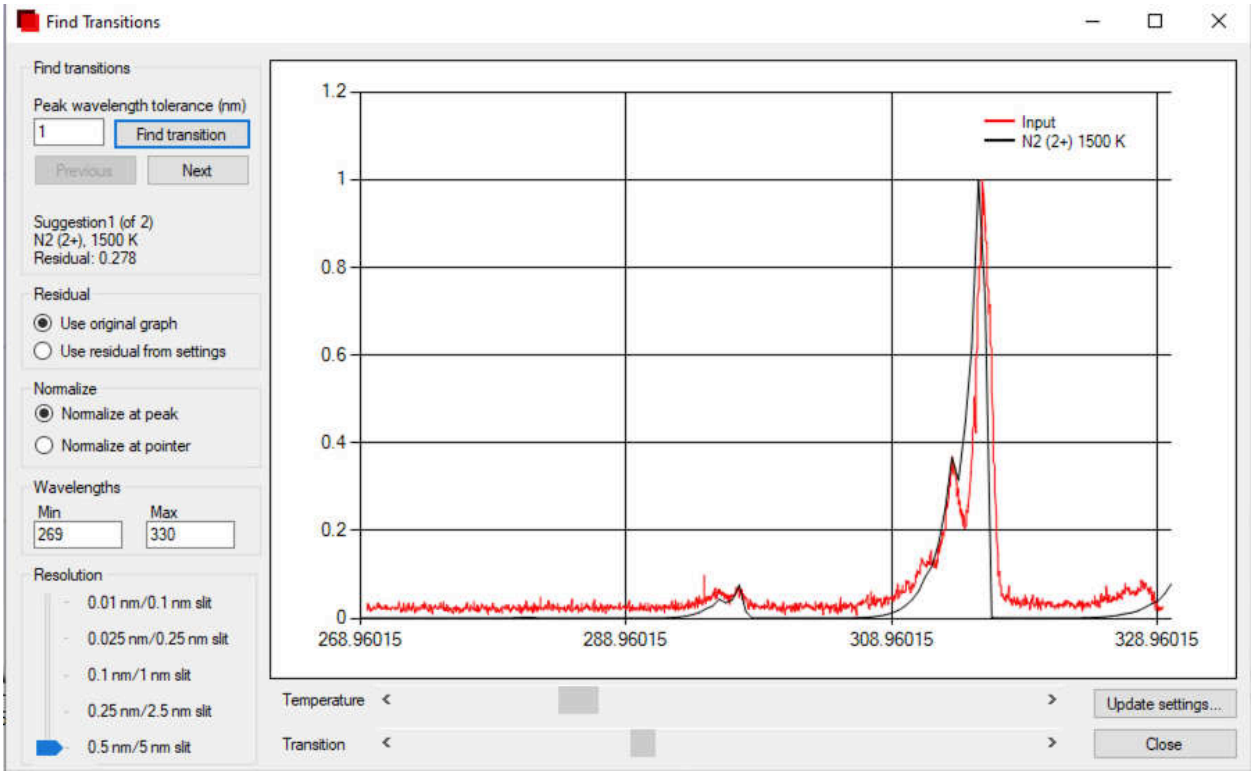

Figure 13. The Find Transitions tool within Specair. Used to identify the molecular transitions present within experimental data. As initial temperature assumption is used to find the best fit.

After the transitions are identified, and the first synthetic spectra is drawn, a wavelength correction is applied that moves the peak of the experimental data to match the peak of the synthetic data. This is shown in Figure 14.

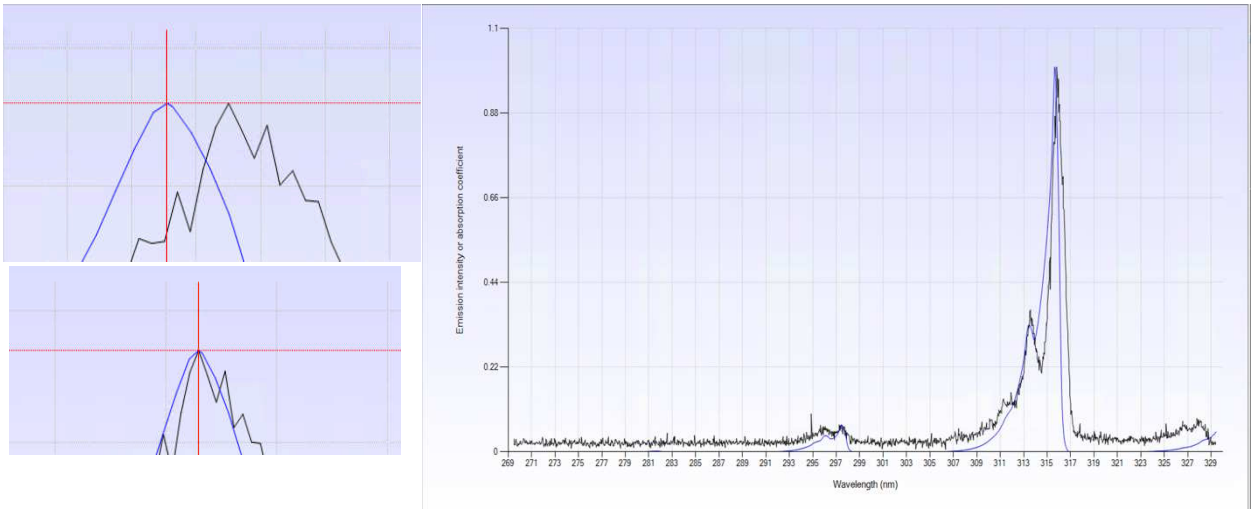

Figure 14. Top Left: The blue curve shows the synthetic spectra generated and the black curve is the experimental. The wavelength of the peak of the synthetic spectra is found, and a shift is applied to the experimental data to match the peak values. Bottom Left: The synthetic spectra and the experimental spectra are now matched peak to peak. Right: The synthetic and experimental spectra overlayed onto one another across the whole image shows good agreement for the two.

This first round of fitting assumes local thermal equilibrium. So, the electronic, rotational, vibrational, and translational temperatures of the species are assumed to be in equilibrium. This is often not the case and variation in these four temperatures can lead to a better fit, quantified by a reduction in the residuals between the experimental and synthetic spectra. Speciar offers the Fit to Spectrum tool which does this. By fixing one of those four temperatures and allowing an optimization algorithm to find the minimum residual, we can converge upon the four temperatures which correspond to the best fit of the data. For example, in Figure 15, the electronic temperature is fixed to 10,000 K whilst the rotational, vibrational, and translational temperatures are free to change but must remain equal to one another. The result is a new temperature of 1517 K. Now, the translational temperature is fixed to 1517 K whilst the rotational and vibrational are free to change but must remain equal to one another. The result is

four different temperatures which produce a minimum in the residual of the synthetic and experimental data. This is graphed in Figure 16.

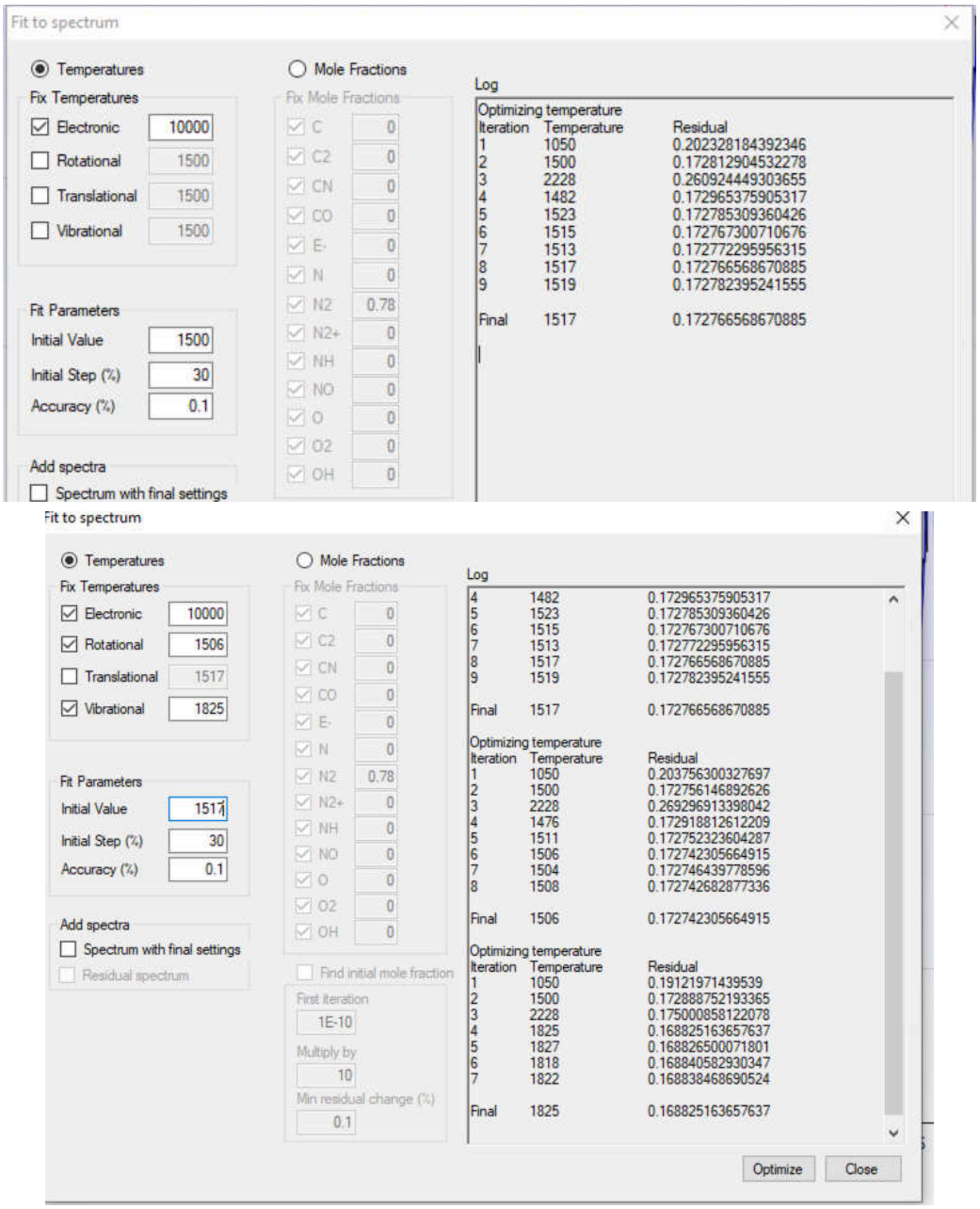

Figure 15. Top: The first round of temperature refinement where the electronic temperature is fixed and the other three are free to move in lockstep with one another, producing a new temperature. This new temperature is then applied to one of the three previously free temperatures as fixed, and the process is repeated until all four temperatures have been optimized.

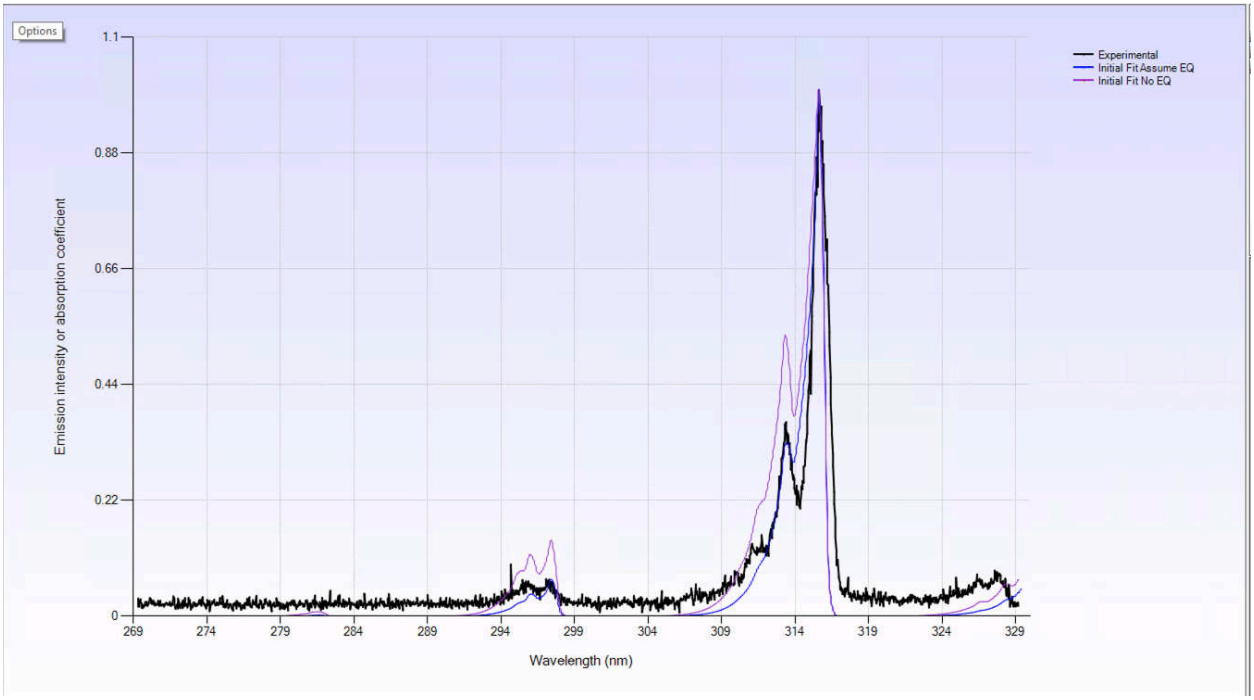

Figure 16. The graphed result of temperature refinement. The blue curve shows the synthetic spectra assuming thermal equilibrium. The purple is the result of allowing all four temperatures to be refined to reduce the residual between synthetic and experimental data.

Temperature refinement can occur for multiple iterations, with each subsequent refinement reducing the residual, but by a diminishing amount. For the work presented herein, the refinement is repeated until the there is no more change in any of the four temperatures when given the opportunity to be optimized. That is, optimization is repeated when any of the four temperatures changes and converges to an absolute minimum when no more temperature change is found through optimization. The result of this repeated optimization is shown in Figure 17.

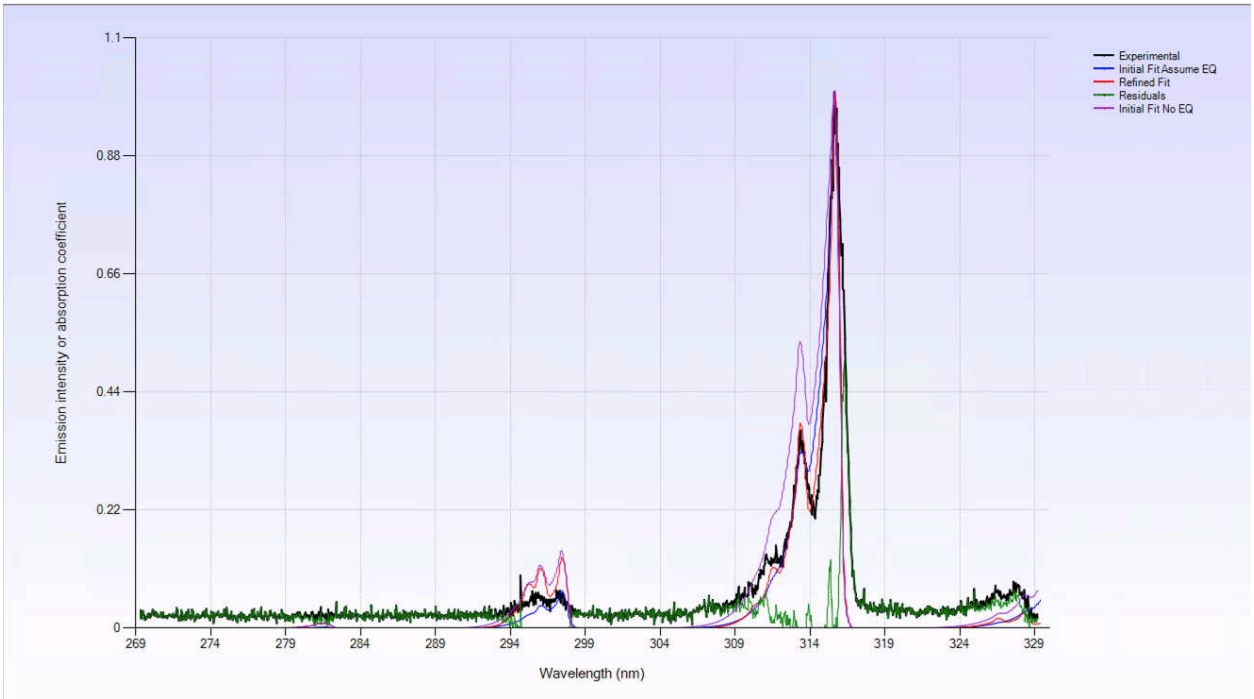

Figure 17. The final refined plot for the synthetic spectra overlaid with all previous iterations. The black curve is the original experimental data. The blue is the initial fit after the transitions are identified. The purple is the result after the first round of temperature optimization. The red is the final fit, after many rounds of temperature refinement until no more temperature changes occur across all four temperatures. The green is the final residuals of the synthetic and the experimental data.

2.5 Plasma Kinetics Modeling

To identify the reaction pathways that are occurring within the plasma generated by the femtosecond laser filament, it is important to be able to model the system using plasma kinetics modeling. Plasma kinetics modeling was accomplished using the zero-dimensional plasma kinetics solver ZDPlasKin [27]. This solver was implemented as a Fortran 90 module that was designed to follow the time evolution of reaction rates, species densities, gas temperatures, and perform sensitivity analysis for a non-equilibrium plasma with arbitrarily complex chemistry. The solver utilizes BOLSIG+ to solve for the reaction rate constants for electron impact reactions and has output files that are compatible with visualizers like QTPlasKin [28–30].

2.5.1 ZDPlasKin Physical Model

ZDPlasKin operates on the following physical model. Consider a species N where the concentration of species N can be denoted as $[N_i]$ where i is the timestep for $i = 1 \ldots \ i_{max}$. To solve for the time rate of change of species N at timestep i, one can use the numerical solution of the balance equation given by,

$$\frac{\mathrm{d[N_i]}}{dt} = \sum_{j=1}^{j_{max}} Q_{ij}(t) \qquad 2\text{-}9$$

where Q_{ij} represents the source or sink terms for all reactions j that create or destroy species N at each timestep i. Consider the following generalized reaction as an example,

$$aA + bB\ [+\delta\epsilon] \rightarrow a'A + cC\ [+\delta\epsilon] \qquad 2\text{-}10$$

where A, B & C are species, $a, b, a',$ & c are mole fractions, and $[+\delta\epsilon]$ is an energy balance term. The reaction rate for this generalized reaction can be computed from

$$\mathrm{R_j} = k_j[A]^a[B]^b \qquad 2\text{-}11$$

where k_j is the reaction rate constant for process j. Therefore, it follows that the source or sink term Q for each species N in the reaction can be given as

$$\mathrm{Q_A} = (a' - a)R;\ Q_B = -bR;\ Q_C = cR \qquad 2\text{-}12$$

These source terms are summed according to Eqn (2-8) at the present timestep i, the change in concentration $\frac{d[N_i]}{dt}$ is applied to the concentrations at the previous timestep $[N_{i-1}]$, and the time evolution of the concentration of species N is tracked. This timestep integration is handled with the DVODE Fortran 90 module. DVODE is a general-purpose double-precision (D) solver that utilizes variable coefficients (V) to solve ordinary differential equations (ODE).

When reactions that involve electron impact are considered, ZDPlasKin invokes the BOLSIG+ solver to compute the rate coefficients. BOLSIG+ is a solver for the electron Boltzmann equation. BOLSIG+ uses the electron energy distribution function (EEDF) to determine rates for ionization, excitation, and attachment reactions based on cross-sectional data. Although effective under normal plasma conditions, the present work found that BOLSIG+ experienced convergence issues in the system of interest, which possessed extreme & rapidly varying species densities. This has created a need for an alternative approach that can handle these unique conditions and provide reliable reaction rates for electron impact reactions. This alternative approach involves the integration of the electron energy distribution function, the cross-sectional area for the reaction, and the velocity of the interacting electron.

2.5.2 EEDF

The electron energy distribution function (EEDF) represents the statistical distribution of electrons across continuous energy levels within a plasma. The EEDF provides insight into the population density of electrons at all energy levels, typically influenced by the electron temperature. At thermal equilibrium, this distribution often follows a Maxwell-Boltzmann form, where the number of electrons decreases exponentially with increasing energy. For the plasma presented in this work, we are assuming a Maxwellian distribution to allow the computation of the EEDF to be given by:

$$\mathcal{F}(\varepsilon, \mathrm{T_E}) = \sqrt{\frac{\varepsilon}{\pi}} 2 \left(\frac{1}{k_B T_E}\right)^{\frac{3}{2}} \exp\left(\frac{-\varepsilon}{k_B T_E}\right) \qquad 2\text{-}13$$

where ε $[eV]$ is electron energy, T_E $[K]$ is electron temperature and k_B $[\frac{eV}{K}]$ is the Boltzmann constant, 8.617×10^{-5}. The final units for the output of the EEDF are $[\frac{1}{eV}]$. However, in non-equilibrium plasmas, the EEDF may deviate from this form due to external factors like electric fields or energy sources, resulting in non-Maxwellian distributions. This could be the case for the

femtosecond filament due to the non-equilibrium conditions establishes throughout the filament lifetime. It is possible that the electrons generated in this method possess a broad energy range that results in an EEDF that reflect individual reaction pathways rather than a Maxwellian distribution. In this case, the EEDF should be obtained experimentally via direct observation or estimated using a non-Maxwellian EEDF calculation. Regardless, this will be explored in future work.

The EEDF is critical in plasma physics as it determines the rates of various electron-driven processes, including excitation, ionization, and dissociation reactions, by describing the likelihood of electrons occupying specific energy states under given conditions.

2.5.3 Cross-section as a Probability

The cross-section as a function of electron energy can be interpreted as the probability of interaction between an electron and a molecule, which depends on the electron's energy and therefore its velocity. This probability reflects the likelihood that an electron, at a given energy level, will undergo a reaction upon encountering a molecule. Generally, higher electron energy corresponds to a reduced cross-section required for interaction; however, if the energy is too high, the electron may bypass the molecule without interacting, as it will not be sufficiently influenced by its presence. Conversely, if the electron energy is too low, interaction may not occur due to insufficient energy to initiate a reaction. This relationship is denoted as σ(ε), where σ represents the cross-section in m^2, and ε is the electron energy in eV. A central hub of electron and ion scattering cross-sections exists in the form of an open-access website called LXCat [31–34].

2.5.4 Reaction Rate Constant Calculation

The kinetic energy of an electron, fundamental to understanding electron-driven reactions, is given by $KE = \frac{1}{2} m_e v^2$ where m_e is the mass of an electron and v its velocity. One

can rearrange this equation and substitute ε for KE to yield $v(\varepsilon) = \sqrt{\frac{2\varepsilon}{m_e}}$. This expression allows us to relate electron energy to velocity, which is crucial when considering electron interactions in a plasma environment. By taking the product of the cross-section σ, the electron energy distribution function (EEDF), and the electron velocity as functions of electron energy $v(\varepsilon)$, we obtain a function that describes the reaction rate for a given electron energy. Integrating this product over the entire energy range yields a single numerical value representing the reaction rate at a specific electron temperature. This integration effectively accounts for the range of energies electrons can have, weighted by both their distribution and the likelihood of interaction with other particles. This equation is given by

$$k(T_E) = \int_0^\infty \sigma(\varepsilon)\mathcal{F}(\varepsilon, T_E)v(\varepsilon)\, d\varepsilon \qquad 2\text{-}14$$

By performing this calculation at various discrete electron temperatures, a temperature-dependent reaction rate can be established. This approach allows one to empirically fit a functional relationship between reaction rate and electron temperature, often expressed in terms of fitting constants.

2.5.5 Arrhenius Rates Curve Fitting

The Arrhenius equation provides a useful form for relating reaction rate to electron temperature, especially when reactions depend strongly on energy thresholds. The Arrhenius equation, traditionally used in chemical kinetics, describes the temperature dependence of reaction rate constants and is given by:

$$k(T) = A \exp\left(\frac{-E_a}{R_U T}\right) \qquad 2\text{-}15$$

where $k(T)$ $[\frac{m^3}{s}]$ is the reaction rate constant, A is the preexponential fitting parameter, E_a is the activation energy of the reaction, and R_U is the universal gas constant. A modified version of this

equation can be used for electron-driven reactions that places more emphasis on the electron temperature T_E given by

$$k(T_E) = AT_E^n \exp\left(\frac{-E_a}{T_E}\right) \qquad 2\text{-}16$$

By adapting the Arrhenius equation to use electron temperature, we can approximate the reaction rate constant as a function of electron temperature. This adaptation is particularly effective when the reaction has a significant activation energy barrier, as is common in processes like ionization or excitation, where only higher-energy electrons can initiate the reaction.

The Arrhenius form captures this threshold behavior by modeling the reaction rate as a rapidly increasing function of electron temperature once the electrons have sufficient energy to overcome E_a. In plasma systems where the electron energy distribution function (EEDF) is non-Maxwellian, fitting reaction rates to an Arrhenius-like model allows the effective reaction rate to reflect both the electron temperature and any deviations in electron energy distribution. This approach provides a convenient, empirically fitted relation that simplifies the complex interaction between electron temperature and reaction rate while maintaining physical accuracy.

Using the Arrhenius equation for reaction rates in this way enables more manageable models of electron-driven processes, allowing simulations to capture temperature-dependent behaviors without the need for explicit integration of cross-section data over the EEDF for every calculation. Thus, the Arrhenius equation serves as a practical and viable approximation for describing the relationship between reaction rate and electron temperature in plasma systems.

CHAPTER 3: FEMTOSECOND FILAMENT EXPERIMENTAL CHARACTERIZATION

3.1 Introduction

This chapter is concerned with the experimental characterization of a laser-induced femtosecond filament in ambient air pressures and conditions. The characterization was performed with optical emission spectroscopy (OES). From the emission spectra that were collected, it has been shown that the inference of gas temperature is possible during the first few nanoseconds after the laser pulse is generated. The primary transitions of interest from the emission spectra were N_2(C-B) and N_2^+(B-X). Further, time-resolved spectral emissions were captured that show the evolution of gas temperature over time and the emission characteristics of the species of interest. Within the N_2 second positive system (N_2(C-B)), it was possible to isolate the first four vibrational levels and observe that a Boltzmann energy distribution was not followed. The focus of these experiments was to study the properties of femtosecond laser plasma primarily for use in pre-ionization. This is contrary to nanosecond laser pulses used in past work for the same purpose.

The rationale for employing femtosecond (fs) pre-ionization is highlighted by the extensive research on laser filamentation in atmospheric air [13,15,35–37]. Studies have demonstrated that plasma filaments can extend over meter-long distances and achieve standoff ranges of several kilometers (e.g. [37] [38]). These systems hold significant interest due to their potential for remote atmospheric sensing through various Lidar techniques, such as pollutant detection via Differential Absorption Lidar (DIAL), as well as applications in laser-guided

This chapter is based primarily on material published as a journal article: V. P. Blanchard, S. Wilson, C. Dumitrache, and A. P. Yalin, "Characterization of a Femtosecond Filament in Air by Optical Emission Spectroscopy," in AIAA Aviation Forum and ASCEND, 2024. My contribution to this was to perform the experiments and analyze the data.

streamers, lightning and discharge generation [39–42], weather modification [43], bow shock control in supersonic flows [44], cavity-free lasing in air [45,46], terahertz radiation generation [47], laser-induced breakdown spectroscopy (LIBS) [48], and flame ignition [49,50].

As discussed in Chapter 2, the formation and propagation of femtosecond filaments are governed by the interplay between Kerr self-focusing, which modifies the refractive index to create a lensing effect that concentrates the light and defocusing due to ionization at the beam's focal point [37,51]. Related studies have also investigated the interaction of nanosecond (ns) pulses with these fs-induced filaments [52–58], offering further insights into the dynamics and applications of laser filaments in air.

3.2 Experimental Setup

3.2.1 Specifications

Figure 18(a) shows a schematic representation of the optical setup and laser paths that were used for experimental investigation. The femtosecond LIP is produced by a Spectra Physics Solstice Ace Laser (centered at 800 nm wavelength, 12 nm bandwidth, 100 fs pulse width) at a 1 kHz repetition rate. The beam was focused with L1 in the schematic, a plano-convex lens with a 750 mm focal length. The average energy per pulse before the filament was 5.9 mJ, and the energy post-pulse was measured to be 5.4 mJ. Thus, the deposited energy into the plasma was 0.5

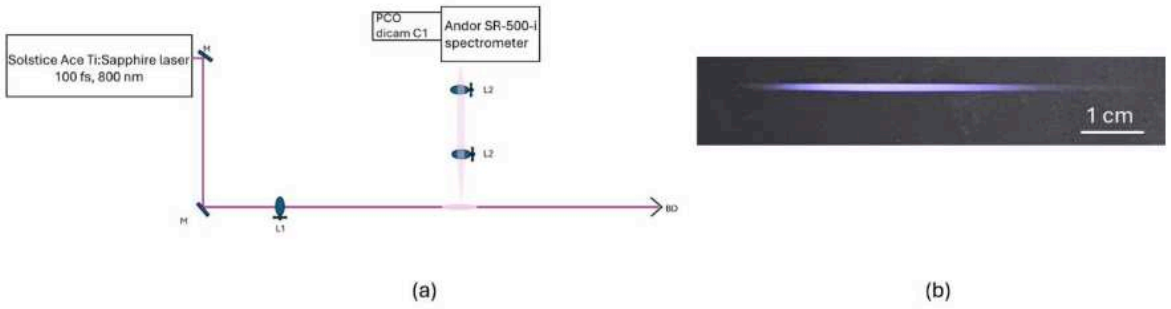

Figure 18. (a) Optical layout showing path of femtosecond laser beam. M (x2): mirror, L1: Plano-convex focusing lens with f=750 mm on translation stage, L2: Plano-convex collection lens with f =75 mm on translation stage, BD: beam dump. (b) Experimental photo of plasma filament generated by femotsecond laser taken with digital camera [11]

mJ/pulse. The length of the filament was roughly 2.5 inches (64 mm) in air at atmospheric pressure, and it's shown in Figure 18(b).

3.2.2 Solstice Ace Laser Assembly

The Solstice Ace laser is a system of lasers that work in tandem with one another to create short-high power pulses from short-low power pulses [59]. A block diagram of the laser is shown in Figure 19. This process is achieved through chirped pulse amplification (CPA). Recall

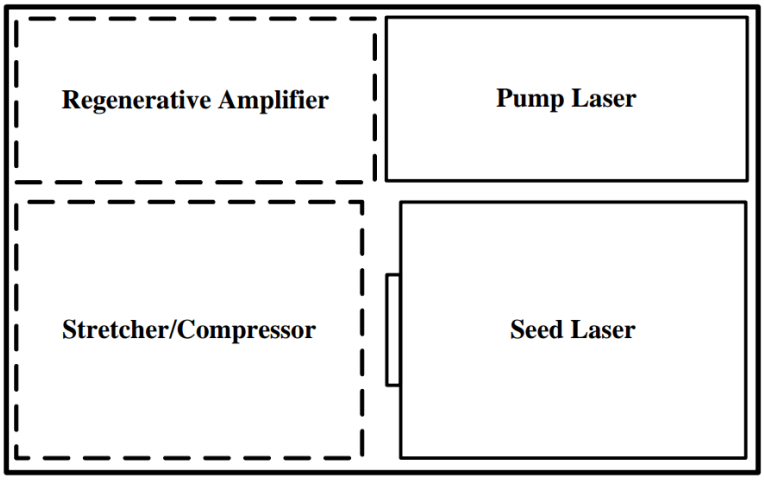

Figure 19. Block diagram of the Solstice Ace laser assembly [59]

from Chapter 2 the process in which a laser self-focuses. When the power exceeds a critical threshold, the refractive index of the air begins to be locally modified, leading to the beam collapsing in on itself and acting as its own focusing lens. Presently, this creates the filament of interest. But it can also happen inside the laser assembly if the power exceeds a critical level. Therefore, CPA is a process that allows the seed pulse to be amplified beyond the peak power of the laser, which would lead to self-focusing. The first step of CPA is to stretch the short-speed pulse, that is to increase its duration, which in turn reduces the peak power of that pulse. This happens in the bottom two compartments of the Solstice Ace laser assembly. The pulse then travels into the regenerative amplifier where a pump laser excites a Ti:Sapphire crystal just before the seed pulse arrives at the crystal. This excitation leads to a population inversion in the crystal which, when the seed pulse passes through, leads to the stimulated emission of the

photons. The stimulated emission amplifies the short seed pulse at the same input wavelength and direction. Finally, the amplified seed pulse passes back through the stretcher/compressor cavity and is reduced back to its original duration. Figure 20 shows the relative size of the pulse as it travels through each compartment of the Solstice Ace assembly.

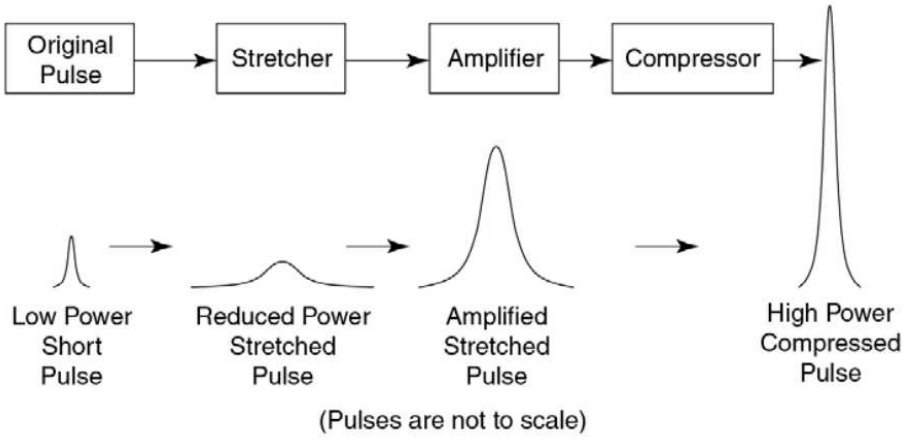

Figure 20. The principle of chirped pulse amplification (CPA) [59]

3.2.3 Intensified Camera

To perform OES diagnostics on the filament, it was necessary to utilize an intensified CMOS (iCMOS)camera. The chosen camera for the present experiments was the PCO Dicam C1. A block diagram of this camera is shown in Figure 21 [60]. An iCMOS camera is an image-intensified camera that can be used to capture low-light events or extremely transient events. At the core of an iCMOS camera is the intensifier, which uses a photocathode to convert incoming photons into electrons via the photoelectric effect. The photocathode in the present case is made of S20, a multialkali material made from sodium, potassium, and antimony. When photons strike the photocathode surface, they transfer their energy to electrons in the material, ejecting these electrons. The number of emitted electrons is proportional to the intensity of the incoming light. The emitted electrons are then accelerated and multiplied using a microchannel plate (MCP). There are several channels within an MCP, and each acts as its own electron multiplier. When an electron enters a channel, it strikes the walls, creating secondary electrons. This cascade effect

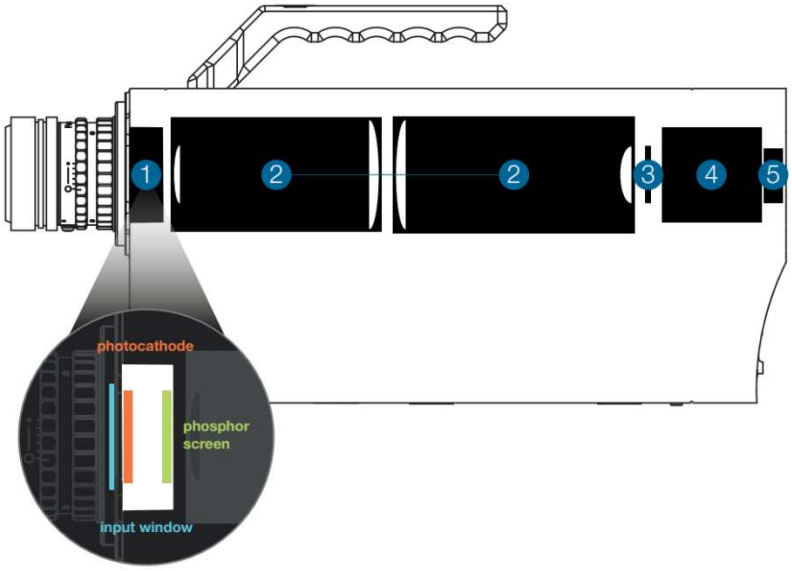

Figure 21. Block diagram of iCMOS Camera (1) the image intensifier, (2) the optical coupling lens system, (3) the sCMOS image sensor, (4) the camera system, (5) the fiber optic interface [60]

amplifies the original electron signal by several orders of magnitude. After amplification, the electron cloud strikes a phosphor screen coated with a material that emits photons when excited by electrons, in this case P46. This step converts the intensified electron signal back into a visible light image. The intensity of the phosphor emission is proportional to the input light signal, preserving the image's brightness distribution. This visible light emitted by the phosphor is captured by the CMOS sensor. The photons generate electron-hole pairs on the sensor, which are converted into a voltage at the pixel level and after processing, are represented as an image. One of the iCMOS camera's defining features is its gating mechanism, which controls the time window during which the image intensifier is active. The MCP or photocathode can be electronically gated on and off within nanoseconds or even picoseconds. This allows the ICCD to capture extremely fast events (e.g., laser pulses or plasmas) with high temporal resolution, effectively freezing motion in time. The camera system was synchronized to the laser output so

that at $t = 0\ ns$ is the first instant at which the emission is detectable by the camera system. The exposure time was kept constant at 2 ns unless otherwise noted, and the final output images were taken as the cumulative average of 15,000 frames.

3.2.4 Spectrometer

The Andor SR-500-i, 0.5-m Czerny-Turner configuration with a 1200-grooves/mm grating blazed at 500 nm was coupled to the iCMOS camera in order to perform OES. A spectrometer operates by directing light through a narrow slit, which serves two key purposes: improving spectral resolution and controlling the amount of light entering the device. The width of the slit plays a critical role in determining the instrument's resolving power. A narrower slit enhances the ability to resolve closely spaced wavelengths, providing finer spectral detail. However, this comes at the cost of reduced light intensity, which can make faint emission bands harder to detect. The trade-off between resolution and light throughput must be carefully balanced for optimal performance. The linear dispersion of wavelengths as a function of position from a given spectrometer is given by the grating equation,

$$\frac{\mathrm{d}\lambda}{\mathrm{dx}} = \frac{d}{mf} \qquad 3\text{-}1$$

where d is the gap between grooves on the diffraction grating, m is the order of from the dispersed light, and f is the focal length of the spectrometer. For present experimentation, the values of $d, m, \& f$ are $\frac{1\ mm}{1200\ lines}, 1, \& 500\ mm$. The resolving power of a spectrometer which determines its ability to distinguish peaks in the spectra is given by the equation,

$$\mathrm{R_{spec}} = \frac{\Delta\lambda}{\Delta x} \times \max(w_1, w_2) \qquad 3\text{-}2$$

where $w_1 \& w_2$ are the widths of the entrance slit, and the width exit slit, which in this case is the width of the pixels in the camera. Clearly, the entrance slit is going to be the maximum between

those two widths. Using a slit width of 150 μm leads to a theoretical maximum resolving power of 0.25 nm. However, when a 632.8 nm HeNe laser was measured, the width of that peak was 0.42 nm.

3.2.5 Wavelength Calibration

To calibrate the spectrometer, we used a two-step approach. The first step is to observe the differences between true wavelength and grating position wavelength by comparing the wavelength the spectrometer is set to against a known calibration source, in this case a Hg:Ar lamp shown in Figure 22.

Figure 22. The discrete spectral lines present in the Mercury (Hg) Argon (Ar) lamp source used for spectrometer calibration.

The Hg:Ar lamp has discrete spectral lines within a broad range of wavelengths. The light from this lamp was collected by the spectrometer to perform our calibration. The spectrometer was set so that one of those spectral lines was imaged on the center of the frame. In actuality, the spectral line of interest is usually off to one side of the center. To account for this, we moved the grating position, that is the set wavelength of the spectrometer, so that the spectral line had its peak at pixel 752, the center of our 1,504 pixel wide image. An example of this is shown in Figure 23 for the discrete spectral line at 546.08 nm.

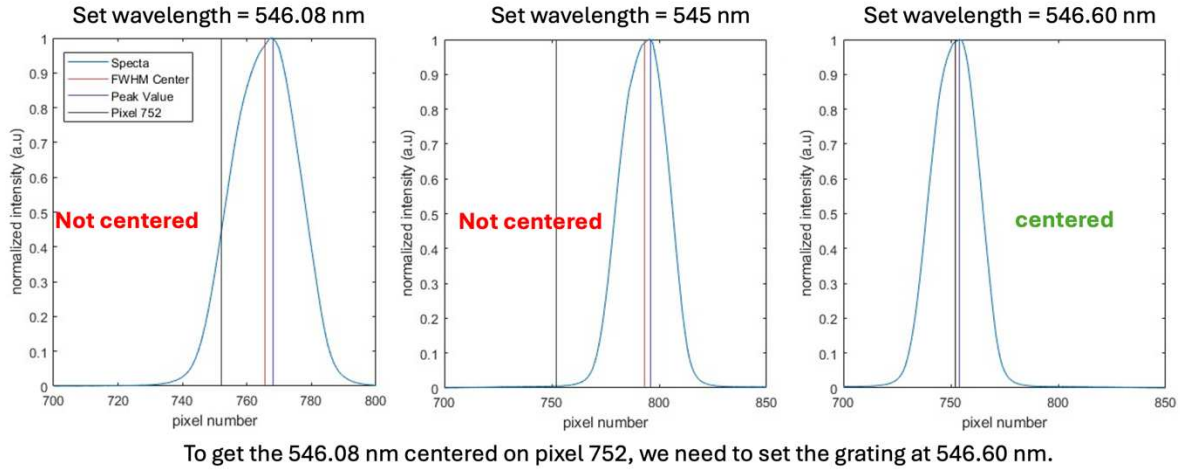

Figure 23. An example of the wavelength correction done for the spectrometer for the spectral line at 546.08 nm.

When the spectrometer is set to the "true" wavelength of 546.08 nm, the full width at half max (FWHM) of the peak is at pixel 765. When the spectrometer is set to a wavelength of 545 nm, the FWHM of the peak is now at pixel 795. When the spectrometer is set to the adjusted wavelength value of 546.60 nm, our spectral line of interest now has the FWHM at pixel 752. The true 546.08 nm spectral line is now centered in the frame when the spectrometer is set to an adjusted value of 546.60 nm. This process was repeated for all the spectral lines of the Hg:Ar lamp as shown in Figure 22 and is graphed in Figure 24. Linear interpolation was performed on the discrete points in the calibration scheme to derive a relationship between set wavelength and

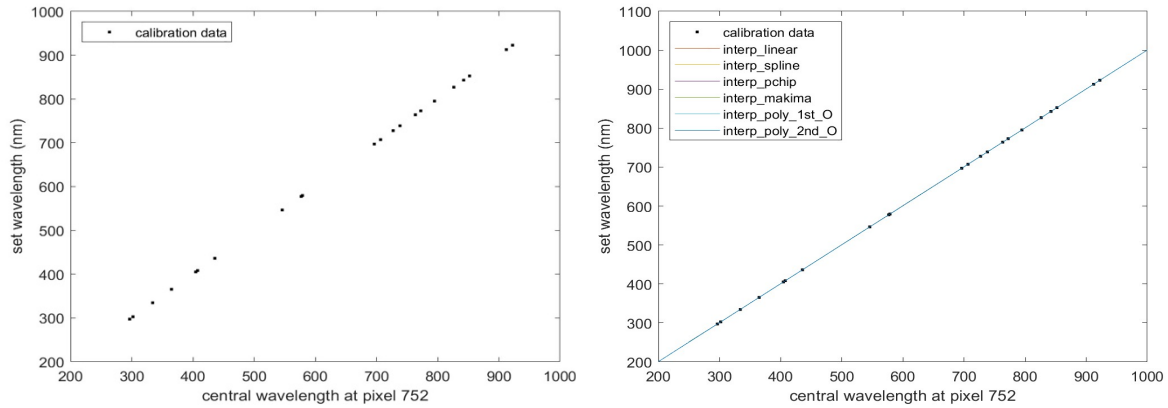

Figure 24. Left: The calibration data from the spectral lines of the Hg:Ar lamp. The set wavelength value (Y-Axis) is what had to be input to the spectrometer so that the central wavelength corresponding to the spectral line of interest (X-Axis) was at the center pixel, 752. Right: A comparison of the linear interpolation methods used to derive a relationship between set wavelength and central wavelength. This interpolation expands the discrete points used for calibration to a function valid for continuous wavelengths.

central wavelength. However, the wavelength values are only calibrated for the center pixel. We still have no notion of what the wavelength values will be at the far image left and right, pixels 0 and 1504. This is the second step of our calibration and is called wavelength dispersion.

If we select three spectral lines across the range of the Hg:Ar lamp, we can derive what the wavelength dispersion is on average across the entire wavelength domain. For each line, we set the grating position such that the line is at the far left side of the image. Due to the work done in step one, we know what the true wavelength is at the center pixel even if the discrete spectral line is not at the center pixel. Thus, if we determine what the pixel number is on the left side of the image where our spectral line is at, we get a set of two lines with known wavelength and pixel numbers. Thus, wavelength can now be computed as a function of any pixel number away from the central pixel. This process is repeated on the right side of the image and for two other spectral lines across the wavelength domain. An example is shown in Figure 25. The 296.73 nm spectral line is placed at pixel 90. The resulting central wavelength is 323.52 nm. Thus, each pixel from 90 to 752 represents a wavelength of 0.04 nm.

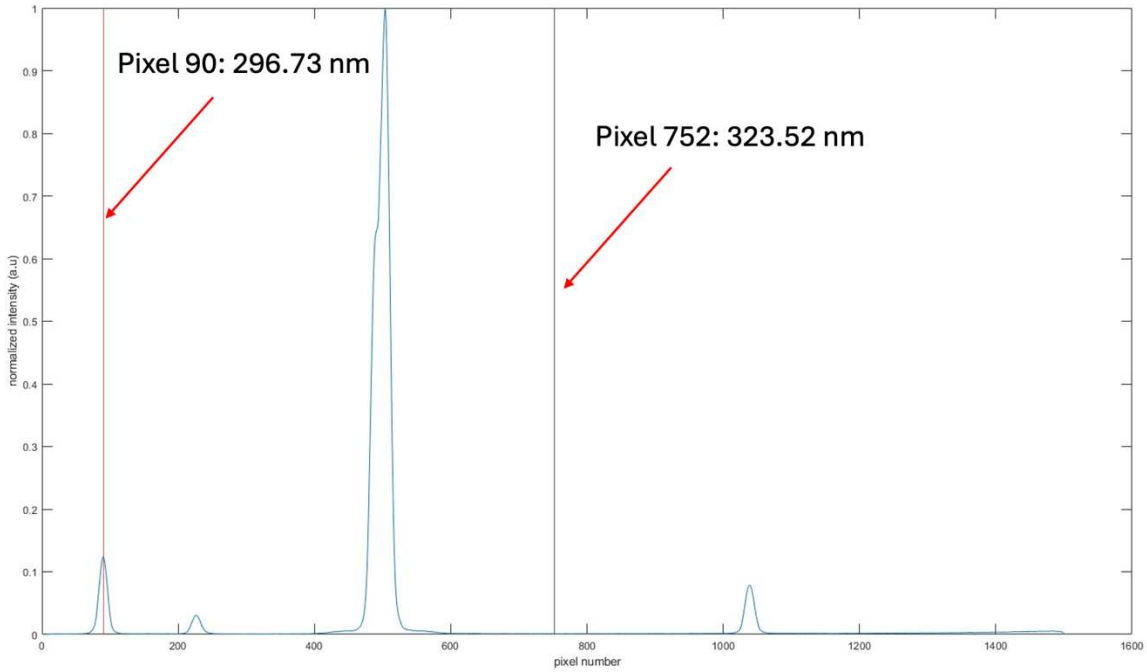

Figure 25. An example of the procedure done to calculate wavelength dispersion across the image.

Now the raw pixel data can be converted first at the center to true wavelength, then using linear dispersion the rest of the pixels in the image can be converted to wavelength. Figure 26

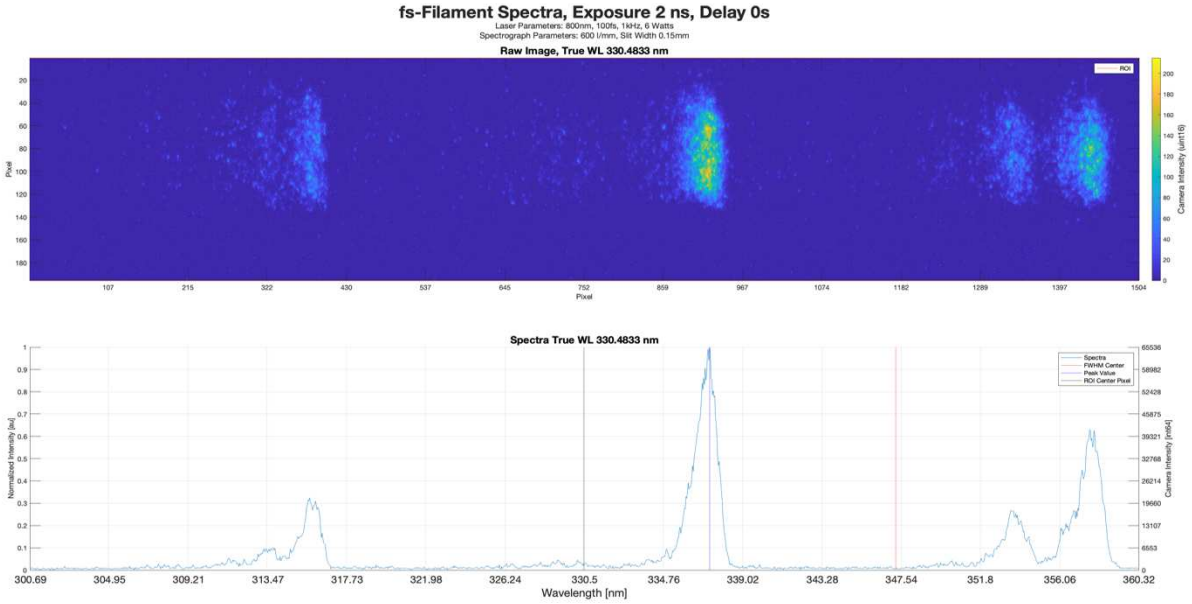

Figure 26. Raw image with pixel axis and converted spectral image with wavelength axis.

shows the raw experimental image with pixel number of the horizontal axis with the corresponding spectral image with wavelength axis beneath it.

3.3 Temperature via Boltzmann Analysis

The radiative code Specair can cross-reference experimental data with a catalog of known energy level transitions as a function of temperature [25,26]. The plasma's rotational and vibrational temperatures was determined during early stages when scattering techniques are less feasible. Specifically, we conduct temperature measurements using the second positive system of nitrogen, N_2 ($C^3\Pi_u \rightarrow B^3\Pi_g$), and the first negative system of N_2^+ ($B^2\Sigma_u^+ \rightarrow X^2\Sigma_g^+$). The second positive system of N_2($C^3\Pi_u \rightarrow B^3\Pi_g$) is a transition from a higher energy level to a lower energy level with associated properties therein. The $C^3\Pi_u$ term describes a triplet excited state (C^3) at a certain electronic level with an associated symmetry (Π_u). Likewise, $B^3\Pi_g$ describes a lower

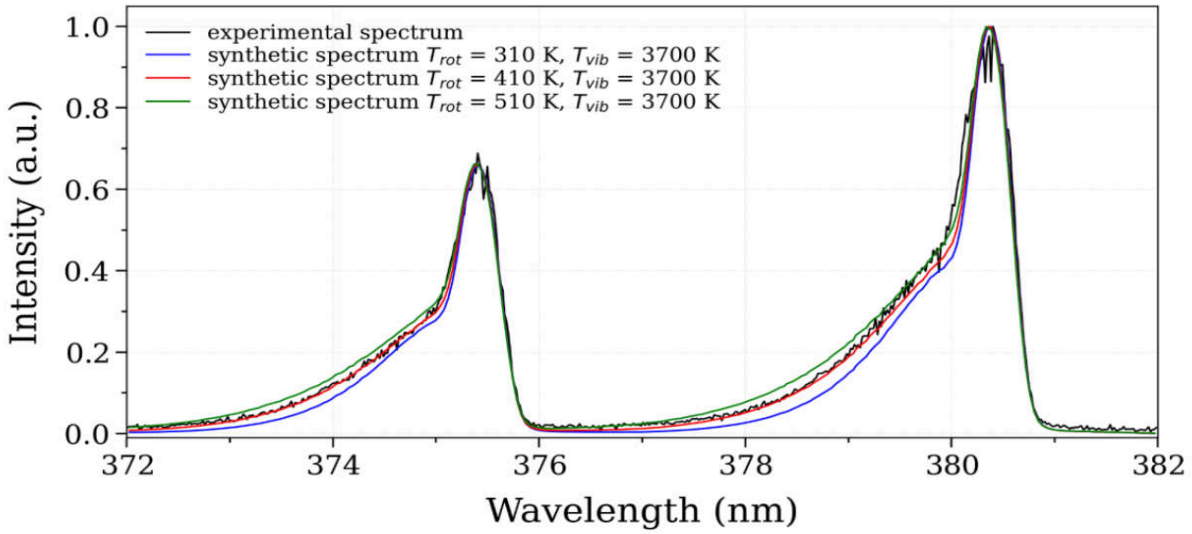

Figure 27. Experimental spectrum of the N_2 second positive system ($\Delta v = -2$) overlayed with three synthetic spectra generated using the plasma emission and absorption code Specair. The best fit corresponds to rotational and vibrational temperatures of T_{rot}=410K and T_{vib}=3700 K respectively. The experimental spectrum was recorded for a femtosecond filament in air at atmospheric pressure and temperature. The spectrum was captured with a 2 ns gate width and a delay of 0 ns relative to filament detection by the camera [11]

triplet excited state ($C^3 \rightarrow B^3$) with a different symmetry (u→g) but the same orbital angular momentum (Π). The experimental spectrum of two vibrational bands of N_2 ($C^3\Pi_u \rightarrow B^3\Pi_g$) (0,2) are shown in Figure 27. Overlayed onto the plot is the corresponding best-fit curve. To illustrate

the rotational temperature uncertainty associated with the fitting process, the figure also includes two synthetic spectra representing rotational temperatures ±100 K from the best fit.

3.4 Chemical Dynamics in Femtosecond LIP Filament

3.4.1 $N_2(C)$ and $N_2^+(B)$ Population and Lifetime

Figure 28 presents the emission spectra of the filament within the 365–400 nm range for delays ranging from 0 ns to 6 ns. The spectra is dominated by molecular emissions from the N_2 second positive system and the N_2^+ first negative system, with no observable continuum which is comparable with what others have seen in similar femtosecond laser-induced plasmas [61–66]. The formation mechanisms of these species remain inconclusive. For $N_2(C)$, three primary pathways have been proposed in the literature. 1) Formation via N_4^+ dissociation. In this scheme, N_4^+ is formed from the association of N_2 and N_2^+, followed by dissociative recombination to produce $N_2(C)$ and N_2, as discussed in Refs. [63,67,68]. 2) An intersystem crossing reaction that is assisted by a collision which starts with multiphoton absorption generating an excited singlet

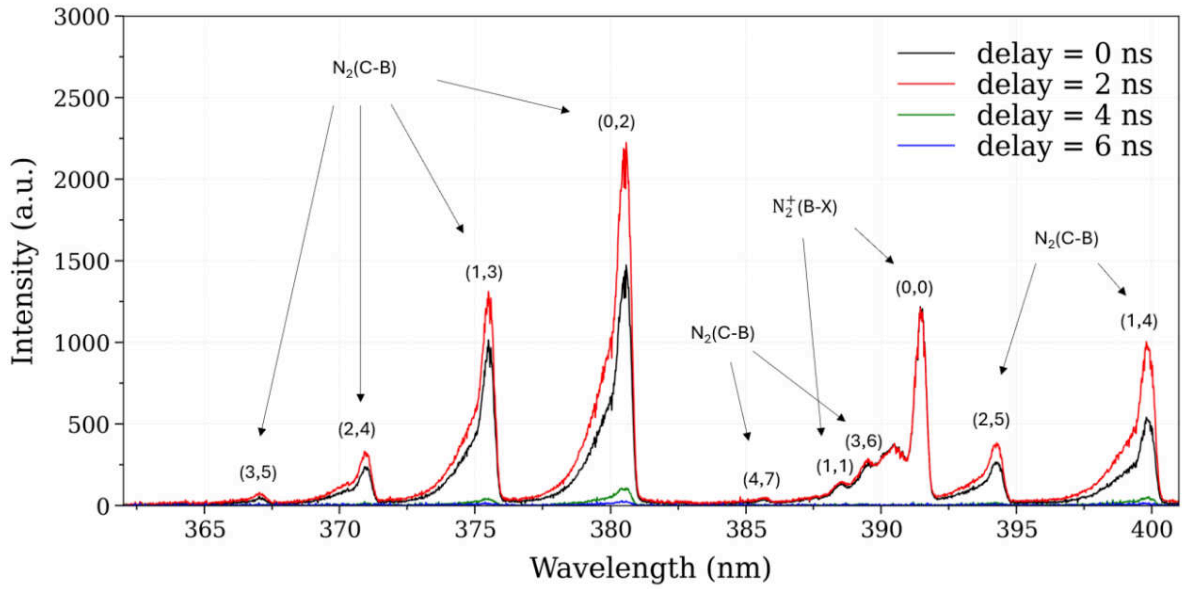

Figure 28. Time resolved experimental spectra of the femtosecond laser-induced filament in standard atmospheric conditions, captured for delays ranging from 0 ns to 6 ns by 2 ns. A delay of 0ns refers to the first instant that emission is visible by the camera. The vibrational band heads of the N_2 second positive system and N_2^+ first negative system are labeled in accordance to the notation (v', v''), where v' represents the vibrational level of the upper electronic state and v'' corresponds to the vibrational level of the lower electronic state [11]

state of N_2, which then undergoes a collision to form $N_2(C)$ [69–71]. 3) Direct electron impact reaction where electron excitation of $N_2(X)$ leads to a population of $N_2(C)$, examined in Refs [66,72–74]. In Chapter 4, the proposed formation mechanisms will be analyzed for $N_2(C)$ through the use of zero-dimensional plasma kinetics modeling. Similarly, the formation of $N_2^+(B)$ has been attributed to several mechanisms. These include multiphoton ionization and tunnel ionization of inner-valence electrons of N_2, as explored in Refs [62,67,70,75,76]. $N_2^+(B)$ can also arise from direct electron-impact excitation of $N_2(X)$ [73] or $N_2^+(X)$ [68].

Figure 29 illustrates the dynamics of these species following their formation, represented by their relative populations. The calculation for relative population is done by using the intensity of the corresponding vibrational band head at a delay of 0 ns and normalizing the subsequent data by that value. That is to say; it shows the relative decay of the species of interest as a function of time after the plasma emission becomes visible. All observable vibrational levels of N_2 (C) show an increase in relative population at a 2 ns delay compared to their values at 0 ns. This suggests that, in addition to the rapid formation mechanisms that populate $N_2(C)$ during the femtosecond pulse within the first few tenths of a picosecond, additional processes are active on the nanosecond timescale under these conditions. One proposed method for the observed rise in emission intensity after the initial filament formation could be attributed to energy pooling reactions involving $N_2(A^3\Sigma_u^+)$ [77]. Beyond this point, the emission intensity of $N_2(C)$ diminishes, becoming undetectable 8 ns after the laser pulse.

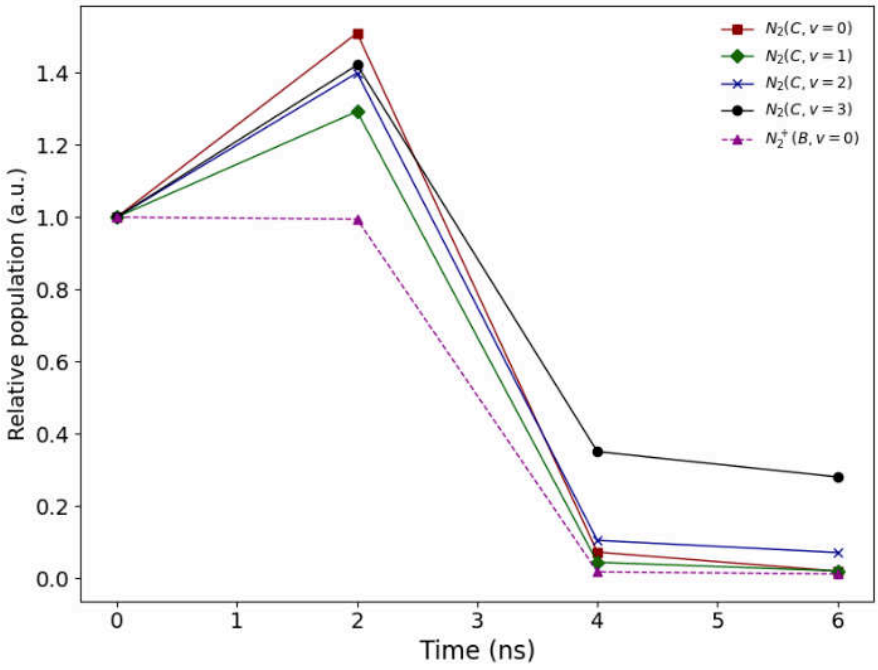

Figure 29. Relative populations of various vibrational states of N_2 excited to the C electronic state and N_2^+ excited to the B electronic state. The relative population of each species is determined via normalization from the emission of the corresponding vibrational band head at a delay of 0ns [11]

The radiative lifetime of $N_2(C)$ is approximately 39 ns, with quenching rate coefficients of about 10^{-11} cm^3/s for N_2 and 2.7×10^{-10} cm^3/s for O_2 [78]. Assuming the populations for N_2 and O_2 are consistent with air at 500 K, the characteristic decay time of $N_2(C)$ due to spontaneous emission and quenching by N_2 and O_2 is roughly 1 ns. This decay time agrees with the experimental behavior observed of $N_2(C)$ and suggests that the dominating destruction reactions for $N_2(C)$ are its quenching with air molecules.

The behavior of $N_2^+(B)$, however, differs significantly. Its population remains steady at delays of 0 and 2 ns but becomes undetectable by 4 ns after the laser pulse. The radiative lifetime of $N_2^+(B)$ is approximately 60 ns, with quenching rate coefficients of 4.6×10^{-10} cm^3/s for N_2 and 6.8×10^{-10} cm^3/s for O_2 [78]. Under the same conditions stated above, the characteristic decay time for $N_2^+(B)$ due to radiative deexcitation and quenching would be about 0.13 ns. The steady population observed at delays of 0 and 2 ns could be explained by competing mechanisms that

both populate and deplete N_2^+(B). After 2 ns, the populating mechanism ceases, and rapid quenching explains its absence after 4 ns.

The plasma filament lifetime of approximately 6 to 8 ns observed here aligns with previous studies using similar focusing conditions with focal lengths ≥ 1 m [55,65,79]. In contrast, studies that utilized focusing optics with a shorter focal length reported plasma emissive lifetimes that followed the trend and were closer to 1 ns [64].

3.4.2 N_2(C) and N_2^+(B) Temperature Measurements

The fitted spectrum shown in Figure 27 allows for the observation of the vibrational temperature of N_2(C) and N_2^+(B) in addition to their rotational temperature of the different vibrational bands observable for the two species of interest. Figure 27 and Figure 30 show that the typical uncertainty for the fit of the rotational temperature for both N_2(C) and N_2^+(B) is around 100 K. The difference in vibrational energy levels $\Delta v = (v', v'')$ can be seen clearly in

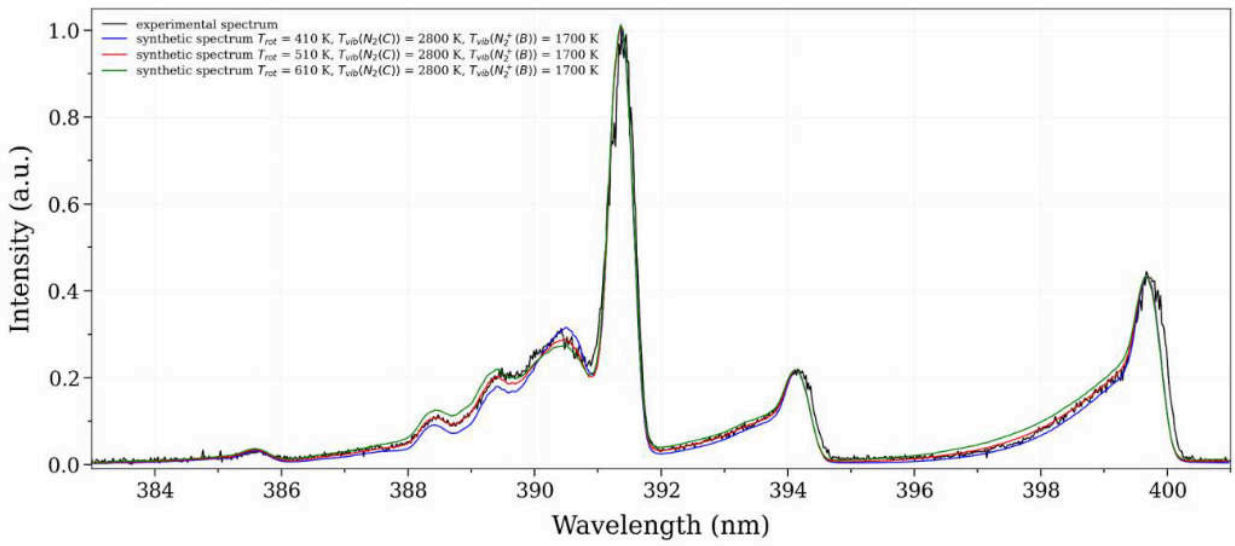

Figure 30. Comparison of a representative experimental spectrum of the N_2 second positive system ($\Delta v = -3$) with three synthetic spectra generated using the line-by-line radiation code Specair. The best fit corresponds to rotational and vibrational temperatures of T_{rot}=510K and $T_{vib}(N_2(C))$=2800 K and $T_{vib}(N_2^+)$=1700 K . The experimental spectrum was recorded for a femtosecond filament in air at atmospheric pressure. The laser deposited 0.5 mJ per pulse into the plasma, operating at a repetition rate of 1 kHz. The spectrum was captured with a 2 ns gate exposure at a delay of 0 ns relative to filament generation [11]

Figure 28 which shows both N_2 systems on the same axes. In Figure 30 the N_2 system with $\Delta v = -3$ is shown whilst in Figure 27 the N_2 system with $\Delta v = -2$ is shown.

The rotational temperature is determined by obtaining the best fit that encompasses two vibrational systems of N_2(C-B) and one vibrational system of N_2^+(B-X), a total of 8 vibrational bands. Figure 31 illustrates that all the fitted rotational temperatures align within the uncertainty of ± 100 K. This suggests that rotational-translational relaxation occurs faster than the characteristic time for spontaneous emission of the N_2 second positive system and the N_2^+ first negative system. Consequently, the rotational temperature determined by global fitting can be assumed to be the same as the gas temperature. Therefore, in our experimental conditions, the gas temperature within the femtosecond filament is approximately 500 K and remains stable throughout the first 6 ns. This temperature is 400 K lower than that observed in a similar setup using a laser energy of 3 mJ [65]. (It should be noted that the laser energy discussed here is different from the energy deposited in the plasma, as elaborated in 3.2.1. While N_2(C) emission is still visible at a 6 ns delay, the quality of the fit at this time does not allow for a reliable determination of the temperature.

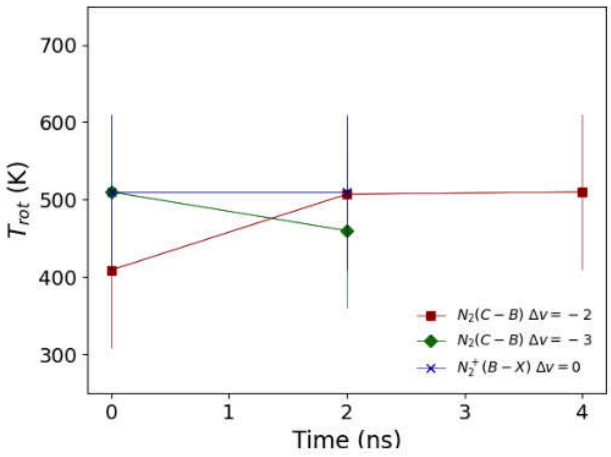

Figure 31. Temperature evolution of the rotational temperature of N_2(C) and N_2^+(B) for the $\Delta v = -3$ & $\Delta v = -2$ systems [11]

The increase in gas temperature up from 300 to 500 K could arise either from cumulative heating caused by the 1 kHz repetition rate of the laser pulses over a long period of time or from heating by a single pulse if the gas has sufficient time to cool back to 300 K between successive pulses. In the latter scenario, the observed 200 K temperature increase would need to occur on a sub-nanosecond timescale. Given the short pulse duration, significant Joule heating is unlikely. Instead, the gas heating may result from processes such as charge exchange reactions, dissociation recombination, or dissociative quenching [80]. Further work is needed to fully understand the mechanisms behind gas heating in femtosecond laser-induced filaments, while the purpose of this work remains on understanding chiefly the reaction pathways for the dominant excited species found in the experimental results, which required a determination of the gas temperatures observed.

The global vibrational temperature of $N_2(C)$ can be analyzed using the spectra shown in Figure 28. However, in Figure 32, it is shown that a single vibrational temperature cannot accurately fit all the visible vibrational bands of the N_2(C-B) ($\Delta v = 2$) transition. The synthetic spectrum assumes a Boltzmann distribution for the vibrational states of $N_2(C)$, indicating that

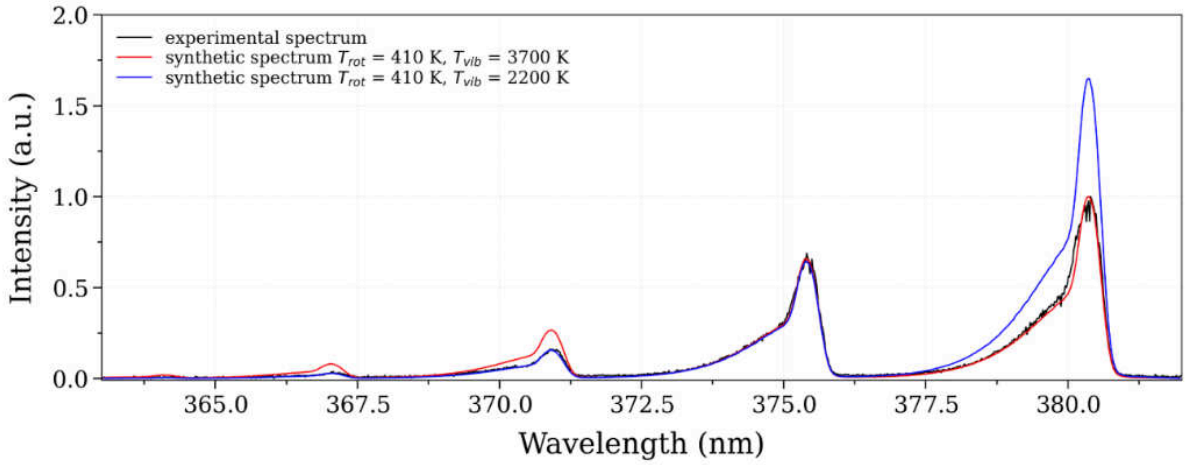

Figure 32. Two fits for the N_2(C-B) transition ($\Delta v = -2$) based on an assumed Boltzmann distribution with different vibrational temperatures to match the various peaks in system [11]

these states do not follow such a distribution. This non-Boltzmann behavior is likely linked to the formation mechanisms of N_2(C), as vibrational-vibrational (V-V) energy transfer occurs on a timescale longer than a nanosecond. As discussed in 3.4.1, the precise mechanisms of N_2(C) formation remain unclear in the literature, with different mechanisms potentially occurring on varying timescales. Energy pooling reactions of N_2(A), suggested as a nanosecond-scale mechanism, could contribute to this process. According to Ref [77], the rate coefficient for energy pooling reactions of N_2(A) that populate N_2 (C, $v = 1$) is 1.6 times higher than for those populating N_2(C, $v = 0$). This aligns with the measurements in Figure 32, where for a vibrational temperature of 2200 K, N_2(C, $v = 0$) is underpopulated. The detailed chemical kinetics for N_2(C) production and destruction are investigated in the next chapter and the energy pooling reactions for N_2(A) after the femtosecond laser pulse are modeled.

CHAPTER 4: MODELING

4.1 Introduction

This chapter will discuss the work done to generate a zero-dimensional model that simulates the time evolution of species within a femtosecond laser-induced filament post-discharge. There is a large emphasis on presenting the methodology for generating the reaction rate constants for various electron-impact reactions as a function of electron temperature. Previous studies have been performed for similar types of modeling that look into the plasma dynamics that occur within femtosecond filamentation. Namely, Shneider *et. al.* have investigated the prospect of tailoring plasma properties to be better suited for dual pulse applications [9]. In this study, the authors found a way to extend the lifetime of femtosecond filaments by overlapping a nanosecond pulse from a neodymium-doped yttrium aluminum garnet (Nd:YAG) laser pulse. The work presented in this thesis differs in that the plasma kinetics mechanism presented herein captures state-specific reactions for excited species of nitrogen and oxygen.

In contrast to the model presented by Shneider *et. al.,* Popov has created a detailed model that does encompass state-specific reactions for nitrogen electronic states [80], although presented for nanosecond electric discharges. This model, which captures dissociative quenching of state-specific nitrogen electronic states through molecular oxygen was verified through experiments by Laux *et. al*. [81]. However, for plasmas generated through the use of a femtosecond laser, very little is known about the plasma kinetics occurring within and few

This chapter is based primarily on material published as a journal article: S. Wilson, V. P. Blanchard, A. P. Yalin, and C. Dumitrache, "Modeling and Experimental Study of Nitrogen Plasma Kinetics in Femtosecond Laser Filaments at Atmospheric Conditions," in AIAA SciTech, 2025. My contribution to this was to generate the model, perform the simulation, and analyze the results.

studies have been performed. The contents of this chapter aim to address that through a combination of modeling of nitrogen and oxygen chemical kinetics and comparison to previously performed optical emission spectroscopy (OES) presented in Chapter 3. The hope is to be better able to describe the time evolution of species within a femtosecond filament and identify reaction pathways for the dominant emissive species observed in the OES data. When a deep understanding of femtosecond plasma chemical kinetics is obtained, it will lead to a furtherance in the readiness of using femtosecond laser-induced plasmas for combustion initiation and propagation in high-performance aerospace engines.

4.2 Zero Dimensional Plasma Kinetics Modeling

In Chapter 2, the equations and physical model used by a program called ZDPlasKin were presented. While such equations will not be repeated for brevity, a general summary of the model is provided. ZDPlasKin takes a species N where the concentration of species N can be denoted as $[N_i]$ where i is the timestep for $i = 1 \dots \ i_{max}$ and solves for the time rate of change of species N at timestep i, via the summation of all the source and sink terms responsible for the generation or destruction of species N. The summation is applied at the present timestep i, and the change in concentration $\frac{d[N_i]}{dt}$ is applied with the concentrations at the previous timestep $[N_{i-1}]$ and the time evolution of the concentration of species N is tracked. Further, the ZDPlasKin solver tracks the time evolution of gas temperature and reaction rates. Within compatible visualizers like QTPlasKin, it is possible to perform sensitivity analyses on the reaction rates to determine formation and loss mechanisms for the species tracked within the model [28–30]. When a reaction involving electron impact is encountered by the solver, BOLSIG+ is employed to calculate the rate constant. This solver has been used effectively in the past to simulate electrical discharges; however the solver was adapted for the present work to handle optical discharges, like those created by femtosecond filamentation. For electrical

discharges, electron-impact reactions are typically characterized by a reduced electric field E/N. To simulate the post-discharge chemical kinetics of femtosecond filaments, this will not suffice as the intensity of the laser post-discharge is null and the reduced electric field likewise is nullified. Thus, a need arises for the derivation of reaction rates as a function of electron temperature. To address this, where normally electron-impact reactions are handed off by the solver to BOLSIG+, we impose computed reaction rate constants through the integration of cross-sectional data found on the LXCat database [82–101] and the electron energy distribution function for a given electron temperature. The results of this integration are then fit to the Arrhenius form and prescribed as inputs to the solver. The methodology for generating such Arrhenius form equations is presented in greater detail in the next section.

4.3 Arrhenius Curve Reaction Rate Constant Generation

Recall Eqn. (2-13) which describes the integration performed to calculate the reaction rate constant k:

$$k(T_e) = \int_0^\infty \sigma(\varepsilon)\mathcal{F}(\varepsilon, T_e)v(\varepsilon)d\varepsilon \qquad 2\text{-}13$$

where $\sigma(\varepsilon)$ $[m^2]$ is the cross-section as a function of electron energy ε $[eV]$. This cross-section can be thought of as a probability for an interaction to occur between a molecule and an electron. The probability is dependent upon the electron's velocity and thus can be related to its energy. Typically, when an electron has high velocity and thus high energy, it requires a lower cross-sectional area to interfere with to start a reaction. However, a critical threshold exists, unique for each reaction, where the electron has excess energy and passes by the potential interaction unphased. On the other hand, if the energy is so low that the electron has inadequate potential to start a reaction the same results as having too much energy is obtained. Thus, a probability is formed where an electron can either interact with a molecule or not dependent upon its energy.

The LXCat database is a comprehensive source for electron and ion cross-sectional data and is open-sourced [31,32,34,91].

The statistical distribution of electrons across continuous energy levels within a plasma can be given by the electron energy distribution function (EEDF) as presented in Eqn (2-12). The population density of electrons as a function of energy is highly influenced by the electron temperature. When a plasma is in thermal equilibrium one can assume a Maxwell-Boltzmann distribution wherein the population of electrons decreases exponentially as energy increases. The plasma investigated in this study will assume a Maxwellian distribution. It is important to note that the plasma generated by femtosecond filaments could deviate from this assumption as a result of the non-equilibrium conditions generated during the laser pulse. Due to the pulse width of femtosecond lasers, a large amount of energy is deposited in a short amount of time which can lead to collisional relaxation being incomplete. Further, the nature of plasma generation for femtosecond lasers being primarily multiphoton ionization (MPI) and electron tunneling ionization exacerbates these conditions. The electrons generated by these mechanisms have a broad range of energy levels and can lead to an alteration of the population as described by the EEDF. In this case, the EEDF should be estimated using non-Maxwellian models or measured directly and will be explored in future work.

Therefore, given the description of the terms in the equation, one can intuit that the numerical output of Eqn (2-13) is a single number that represents the reaction rate constant for a given reaction at a given electron temperature. By computing this reaction rate constant at a variety of discrete electron temperatures, we can create an empirical fit of reaction rate constants as a function of temperatures. The Arrhenius equation provides a good framework for us to build our relationship between reaction rate constant and electron temperature. Recall equation (2-15)

which was a modified version of the Arrhenius equation that places more emphasis on the electron temperature T_e $[K]$:

$$k(T_E) = AT_E^n \exp\left(\frac{-E_a}{T_E}\right) \left[\frac{cm^3}{s}\right] \quad \textit{2-15}$$

where $A, E_a, \& \, n$ are the fitting constants. By modifying the Arrhenius equation to incorporate electron temperature, the reaction rate constant can be approximated as a function of electron temperature. This adaptation is particularly effective for reactions with significant activation energy barriers, such as ionization or excitation, where only higher-energy electrons can trigger the reaction. The Arrhenius form captures this threshold behavior by modeling the reaction rate as a rapidly increasing function of electron temperature once electrons possess sufficient energy to overcome E_a. This approach provides an empirically fitted relation that simplifies the complex interaction between electron temperature and reaction rate while maintaining physical accuracy. Using the Arrhenius equation in this manner enables more manageable models of electron-driven processes, allowing simulations to capture temperature-dependent behaviors without requiring explicit integration of cross-section data over the EEDF for each calculation. Thus, the Arrhenius equation offers a practical and efficient approximation for describing the relationship between reaction rate and electron temperature in plasma systems.

4.4 Arrhenius Curve Fitting MATLAB Code

A MATLAB code was written that computes the equation for the electron temperature-dependent reaction rate constant k in the form of Eqn (2-15). This code imports the cross-sectional data from the LXCat database and applies a smoothing spline to interpolate between data points. This was done to allow for higher fidelity numerical integration to occur when calculating the integral form of the reaction rate constant given by Eqn (2-13). The code uses

nonlinear least squares regression via the MATLAB function $fminsearch()$ to compute the values of the fitting parameters $A, E_a, \& n$ that reduces the sum of the squared errors between the computed data points and the fitted curve evaluated at those points to a minimum value. The procedure used to obtain the reaction rate constant Arrhenius curve is depicted graphically in

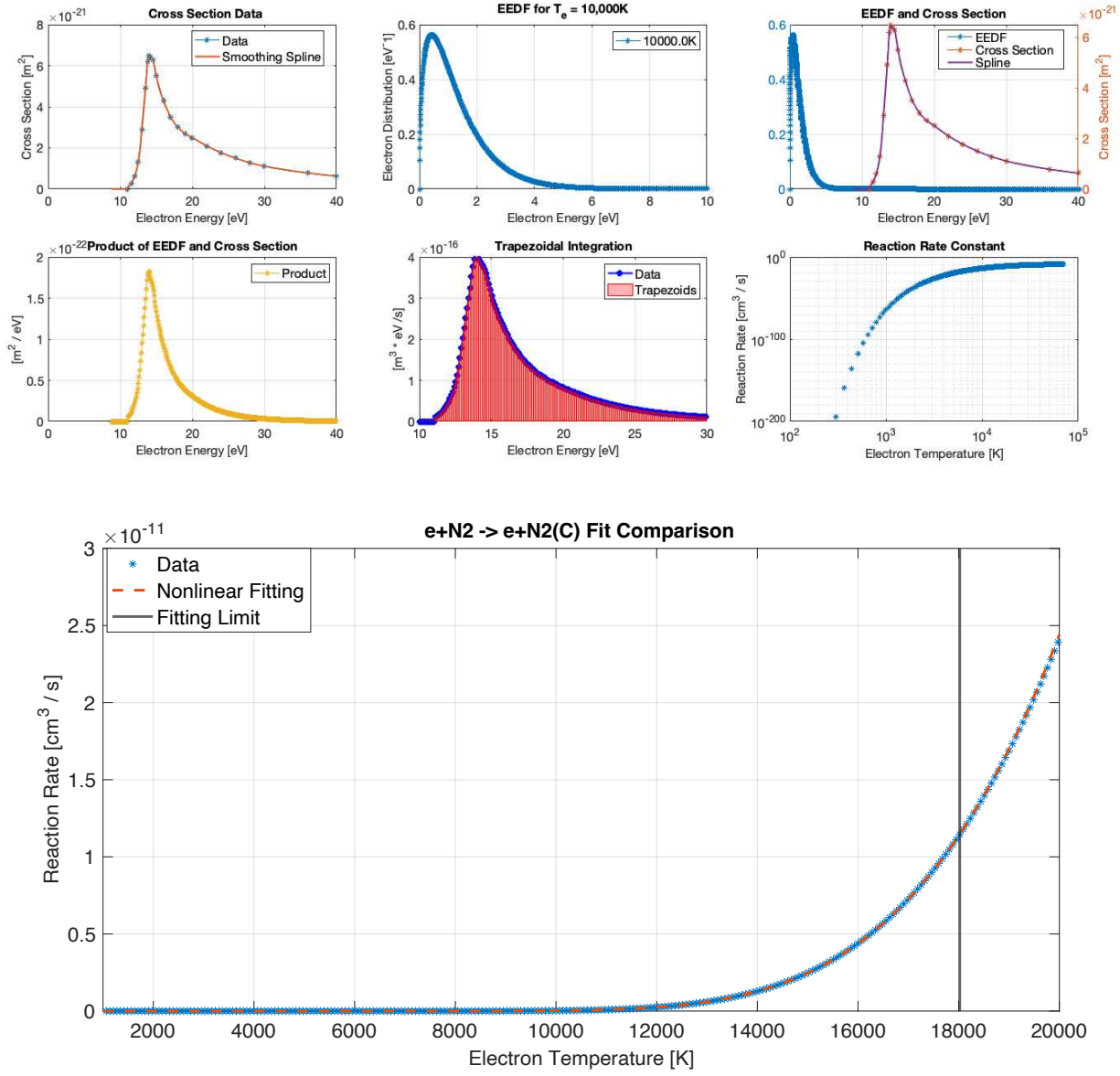

Figure 33. Top: Graphical representation of the steps taken to obtain the reaction rate constants in the Arrhenius form.

Bottom: An example of the nonlinear fitting that was performed to obtain the reaction rate constant calculations of the electron-impact reaction e+N_2(X) -> N_2 ($C^3\Pi_u$) +e. The vertical gray line indicates at what point the Arrhenius curve fit is limited to when performing optimization. This was done to improve the accuracy at lower temperatures.

Figure 33-Top for the reaction $e + N_2 \rightarrow N_2(C) + e$ where the subplots show the $\sigma(\varepsilon)$ fitted with a spline, the computed Maxwellian EEDF for a given T_e, an overlay of $\sigma(\varepsilon)$ with $\mathcal{F}(\varepsilon, T_e)$ to visually show the product of those two curves, the trapezoidal integration process prescribed in Eqn (2-13), and the computation of the reaction rate constant k at discrete values for T_e. Finally, the nonlinear Arrhenius curve fitted to the discrete values of k is shown in Figure 33-Bottom. This curve serves as the input value for the ZDPlasKin solver.

To validate the accuracy of this fitting process, a comparison was made between the reaction rate constants computed from the Arrhenius form and the BOLSG+ computed reaction rate constants for a nanosecond repetitively pulsed discharge (NRP) simulation. The result of that comparison for nitrogen reactions is shown in Figure 34, oxygen reactions in Figure 34, and NO_x reactions with electron number density in Figure 36.

When performing the validation, it was necessary to focus on the lower temperature regimes (below 1.5 eV or ~17,400 K) within the fit to obtain more accurate Arrhenius form equations. This need came from an observed overestimation of the species densities when compared to the values nominally computed by BOLSIG+.

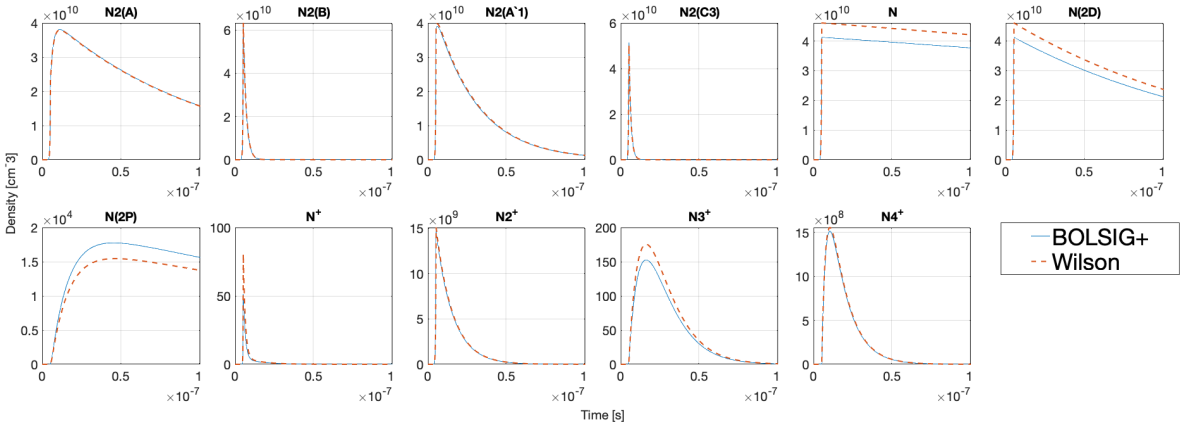

Figure 34. Species number density comparison for nitrogen electron impact reactions. The Arrhenius form reaction rate constants and BOLSIG+ computed reaction rates served as the inputs for the computed species densities. The blue curve depicts what is computed by BOLSIG+ and the orange dotted curve the values from the Arrhenius rate input. The simulation is performed for a NRP at atmospheric conditions for an initial temperature of 1200K.

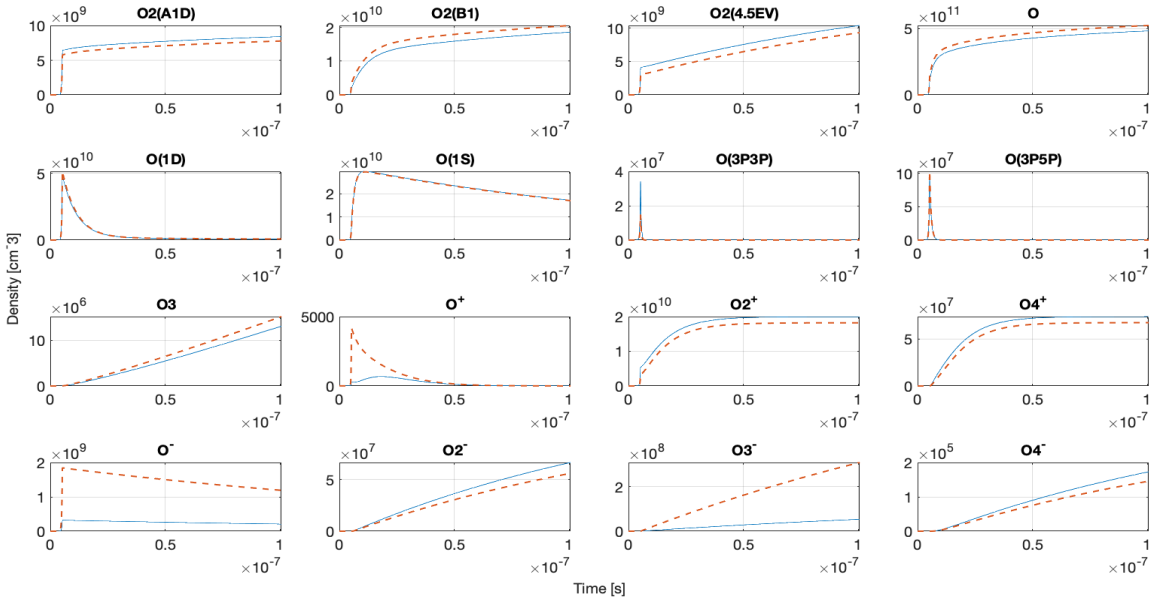

Figure 35. Species number density comparison for oxygen electron impact reactions. The Arrhenius form reaction rate constants and BOLSIG+ computed reaction rates served as the inputs for the computed species densities. The blue curve depicts what is computed by BOLSIG+ and the orange dotted curve the values from the Arrhenius rate input. The simulation is performed for a NRP at atmospheric conditions for an initial temperature of 1200K.

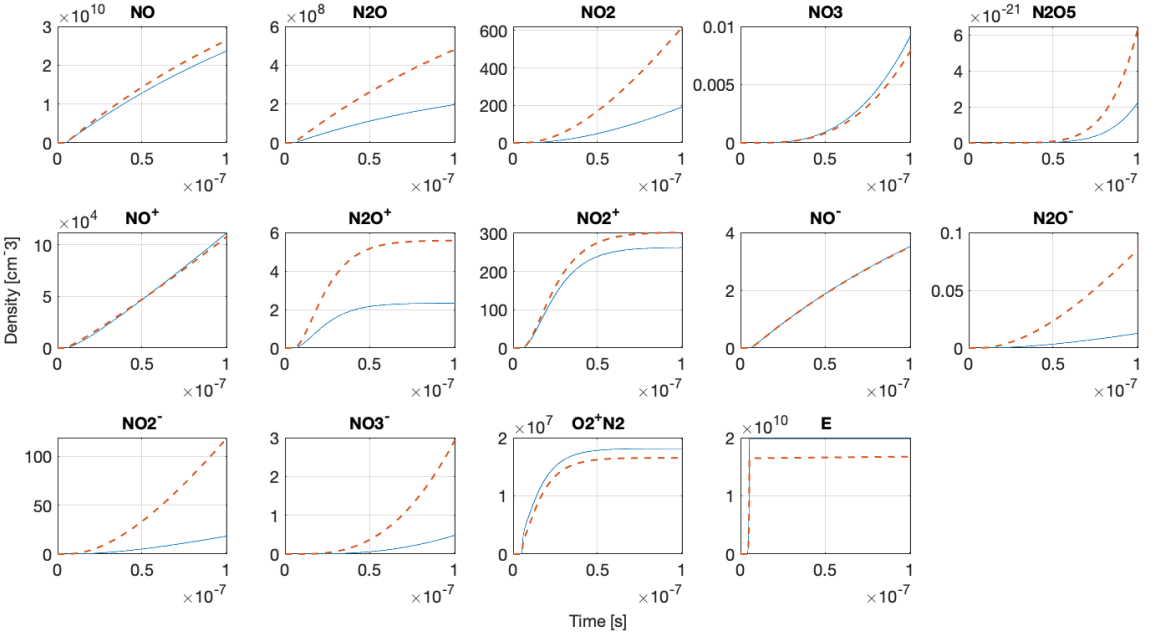

Figure 36. Species number density comparison for NO_X electron impact reactions. The Arrhenius form reaction rate constants and BOLSIG+ computed reaction rates served as the inputs for the computed species densities. The blue curve depicts what is computed by BOLSIG+ and the orange dotted curve the values from the Arrhenius rate input. The simulation is performed for a NRP at atmospheric conditions for an initial temperature of 1200K.

When the nominal temperature range seen for NRP plasma was used (1,000 – 70,000 K) the Arrhenius fit appeared to be valid for all temperatures. That is, the fitted curve appeared to intersect all computed data points. However, a deviation existed in the lower temperature region.

Using the knowledge that the maximum electron temperature produced by the femtosecond filament is 1 eV or 11,606 K, it makes physical sense to impose a fitting limit for the lower temperature regime for the femtosecond reaction rate constants [5]. This fitting limit is depicted by the vertical gray line in Figure 33-Bottom. The deviation and the improvement made by imposing the limit are shown in Figure 37.

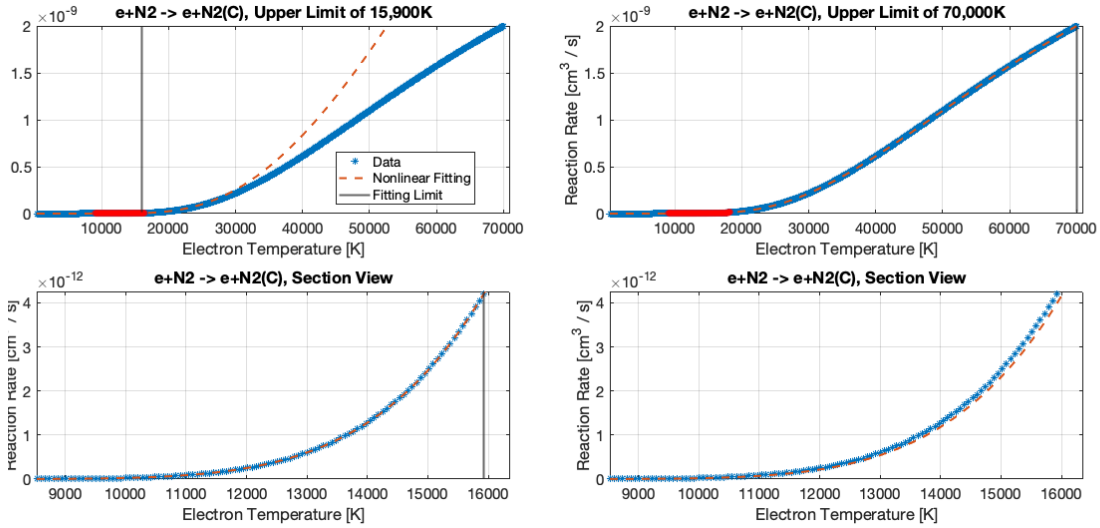

Figure 37. A comparison of the effect of the imposed fitting limit on the nonlinear fitting data. The top row shows the same set of data fit with two different limits, shown with the vertical gray line. The bottom row shows a zoomed section of the top two plots (highlighted red in the top row) which demonstrates that adjusting the fitting limit improves the fit at lower temperatures.

The chemical kinetics model for the femtosecond filament plasma evolution in the post-discharge phase is built upon the reaction rates proposed by Capitelli *et. al.* [101] and Ivanov *et. al.* [68]. As stated previously, the electron-impact reactions previously solved with the help of BOLSIG+ are now replaced with the Arrhenius form of Eqn (2-15) and in accordance with the fitting parameters found in Table 1.

Table 1: Arrhenius Parameters for Electron Impact Reactions

Reaction Number	Reaction	A	Ea	n
1	$e + N_2 \rightarrow e + N_2(A, v = 0-4)$	1.77E-13	7.59E+04	0.704
2	$e + N_2 \rightarrow e + N_2(A, v = 5-9)$	7.97E-12	8.59E+04	0.498
3	$e + N_2 \rightarrow e + N_2(A, v \geq 10)$	4.92E-11	9.75E+04	0.346
4	$e + N_2 \rightarrow e + N_2(B)$	4.74E-10	8.94E+04	0.243
5	$e + N_2 \rightarrow e + N_2(W)$	2.99E-11	9.41E+04	0.494
6	$e + N_2 \rightarrow e + N_2(B`)$	8.81E-12	9.78E+04	0.514
7	$e + N_2 \rightarrow e + N_2(a`)$	3.00E-12	9.59E+04	0.564
8	$e + N_2 \rightarrow e + N_2(a)$	5.59E-11	9.50E+04	0.352
9	$e + N_2 \rightarrow e + N_2(w)$	2.42E-12	1.05E+05	0.711
10	$e + N_2 \rightarrow e + N_2(C)$	1.60E-09	1.34E+05	0.257
11	$e + N_2 \rightarrow e + N_2(E)$	1.09E-08	1.23E+05	-0.336
12	$e + N_2 \rightarrow e + N + N(2D)$	7.66E-11	1.55E+05	0.541
13	$e + O_2 \rightarrow e + O_2(a1D)$	4.82E-13	1.43E+04	0.715
14	$e + O_2 \rightarrow e + O_2(b1)$	9.98E-15	1.72E+04	1.013
15	$e + O_2 \rightarrow e + O_2(4.5eV)$	2.13E-05	7.25E+04	-0.852
16	$e + O_2 \rightarrow e + O + O$	8.50E-11	6.65E+04	0.464
17	$e + O_2 \rightarrow e + O + O(1D)$	4.33E-01	1.08E+05	-1.439
18	$e + O_2 \rightarrow e + O + O(1S)$	1.09E-11	1.13E+05	0.375
19	$e + O_2 \rightarrow e + O + O(3p3p)$	4.31E-12	1.86E+05	0.296
20	$e + O_2 \rightarrow e + O + O(3p5p)$	5.30E-12	1.84E+05	0.423
21	$e + O \rightarrow e + O(1D)$	8.24E-14	2.15E+04	1.140
22	$e + O \rightarrow e + O(1S)$	1.99E-12	4.92E+04	0.560
23	$e + O \rightarrow e + O(3p3p)$	3.17E-11	1.28E+05	0.446
24	$e + O \rightarrow e + O(3p5p)$	2.17E-11	1.26E+05	0.408
25	$e + N \rightarrow e + e + N^+$	1.25E-09	2.48E+05	0.346
26	$e + O \rightarrow e + e + O^+$	3.16E-12	1.53E+05	1.005
27	$e + N_2 \rightarrow e + e + N_2^+$	2.60E-11	1.82E+05	0.579
28	$e + O_2 \rightarrow e + e + O_2^+$	9.34E-12	1.37E+05	0.580
29	$e + O_2(a1D) \rightarrow e + e + O_2^+$	5.11E-11	1.24E+05	0.594
30	$e + N_2O \rightarrow e + e + N_2O^+$	5.55E-12	1.46E+05	0.706
31	$e + O_2 \rightarrow O^- + O$	6.40E-13	5.68E+04	0.655
32	$e + NO \rightarrow O^- + N$	6.37E-13	5.67E+04	0.335
33	$e + O_3 \rightarrow O^- + O_2$	6.79E-15	3.34E+02	1.345
34	$e + O_3 \rightarrow O_2^- + O$	1.69E-08	8.00E+03	-0.308

Table 2: Associative Combination and Quenching Reactions for N_2^+ and N_4^+, from Ivanov et. al. [68]

Reaction Number	Reaction	$k\ [cm^3/s]$
35	$N_2^+ + 2e \rightarrow N_2 + e$	6.35×10^{-25}
36	$N_2^+ + N_2 + e \rightarrow 2N_2$	5.29×10^{-30}
37	$N_4^+ + e \rightarrow N_2(C) + N_2$	1.70×10^{-6}
38	$N_2^+ + e \rightarrow N + N$	1.34×10^{-7}
39	$N_2^+ + 2N_2 \rightarrow N_4^+ + N_2$	1.00×10^{-28}
40	$N_2^+ + O_2 + N_2 \rightarrow NO^+ + N_2 + NO$	[102,103]
41	$N_2^+ + O_2 \rightarrow NO^+ + N + O$	8.00×10^{-10}
42	$N_2^+ + N_2 \rightarrow N + N_3^+$	3.00×10^{-10}
43	$N_4^+ + e \rightarrow 2N_2$	4.90×10^{-7}
44	$N_4^+ + N_2 \rightarrow N_2^+ + 2N_2$	8.30×10^{-13}

Table 3: Quenching and Excitation of N_2, and Optical Transitions, from Capitelli **et al.** *[101]*

Reaction Number	Reaction	$k\ [cm^3/s]$
45	$N_2(A) + N_2(A) \rightarrow N_2 + N_2(C)$	1.50×10^{-10}
46	$N_2(C) + N_2 \rightarrow N_2(a`) + N_2$	1.00×10^{-11}
47	$N_2(C) + O_2 \rightarrow N_2 + O + O(1S)$	3.00×10^{-10}
48	$N_2(C) \rightarrow N_2(B)$	2.45×10^{7}

4.5 Simulation Initial Conditions

The simulation performed in this study begins at the end of the femtosecond pulse, which is not modeled here but rather references the work of others [5,9]. Rather, the post-discharge conditions are determined using the assumed clamped intensity value (refer to section 2.2.2) of $I = 5 \times 10^{13}$ W/cm^2 for self-focusing laser in atmospheric air with a species density of $n = 2.5 \times 10^{19}$ molecules/cm^3, based on [38]. Knowing that the pulse width is 100 fs, electron avalanche plasma formation is neglected as well as dissociative and associative ionization processes. The characteristic time for these processes to occur at atmospheric pressure is much longer than the pulse width of the laser, as described in Eqn (2-2). Rather, work performed by Talebpour [104] allows us to determine the rate of MPI ionization within the fs-pulse and to infer the species density of nitrogen and oxygen ions as reported in Table 4. Using an analytical method proposed by Mur *et. al.*, the generation of photoelectrons under strong radiation

conditions within femtosecond pulses is found, and the electron temperature of the filament is obtained via EEDF calculations [105]. Finally, given the restraint that ZDPlasKin does not allow a time-evolved EEDF calculation, the post-pulse electron temperature used in the present work was derived from previous work done by others in our lab and is outlined in Ref [5] and shown in Figure 38. The steep nature of the curve at early timesteps calls for linear interpolation to occur in the timesteps immediately following the start of the simulation. The time domain in which our simulation exists takes place after the pulse has ceased therefore the reduced electric field E/N has also ceased. Through the combination of the time-resolved electron temperature derived from others and the initial species densities calculated immediately after the pulse from previous studies, the foundation upon which our post filament femtosecond simulations is laid.

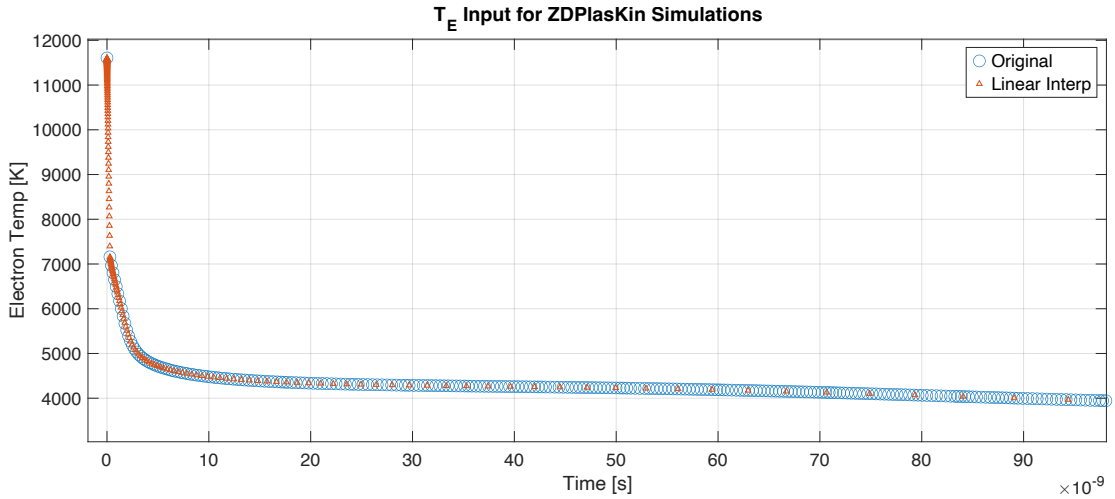

Figure 38. Discrete electron temperature values, serving as a input to the ZDPlasKin simulation. Derived from EEDF calcuations done by Hooyshar et al. *shown in blue. The orange datapoints are the result of a linear intepolation to provide more timesteps at earlier simulation times where the plasma chemistry is most important [5].*

Table 4 Initial Densities of Species Post Femtosecond Filament [5]

Species	Initial Number Density $[1/cm^3]$
e	1.024×10^{17}
N_2	1.650×10^{19}
O_2	8.280×10^{18}
N_2^+	4.080×10^{14}
O_2^+	1.020×10^{17}

4.6 Results

4.6.1 Spectra Differences Between Femtosecond and Nanosecond LIP

In Chapter 3, the results of OES and the emission spectra for femtosecond laser-induced plasma are shown. In Figure 28 the spectra is dominated by the molecular emission from the N_2(C-B) and N_2^+(B-X) transition. Further, strong emission is present from the triplet of atomic oxygen (at 777 nm) and excited (O^+ at 470 nm), but those atomic lines are not the focus of this study. Throughout the spectra, no continuum is observed. These results differ from the spectra of those collected for nanosecond laser-induced plasmas. The spectra for the nanosecond variety shows a strong continuum, the absence of molecular emission, and typically are detectable into the tens of microseconds [10,106]. As a direct comparison between femtosecond and nanosecond spectra, previous studies utilizing nanosecond laser breakdown have seen faint emission for the N_2(C-B) and N_2^+(B-X) transition, albeit delay times longer than 1 μs [107]. Recall that the delay times at which the N_2(C-B) and N_2^+(B-X) emission is no longer visible is 6 ns for femtosecond-induced plasma. In further contrast, the nanosecond laser spark emission spectra for delay times of the same caliber are dominated by Bremsstrahlung radiation coming from free electrons in the plasma.

That is not to say there are no similarities between the two sets of laser-induced plasmas. In the case of NRP, both femtosecond filaments and NRP show a strong emission for N_2(C-B) and N_2^+(B-X) at early times. This could indicate a lower degree of ionization and dissociation within NRP than in a nanosecond spark. However, the emission time for such a transition is still much shorter in femtosecond filaments than in NRP [81]. Therefore, the need to understand the complex chemical kinetics acting in femtosecond filaments is furthered by its differences against nanosecond laser breakdown, nanosecond sparks, and NRP.

4.6.2 Proposed Formation Mechanisms for $N_2(C)$

Previous studies have shown that similar optical setups to produce femtosecond filaments have spectra emissions that are dominated by N_2(C-B) [61–66]. Within these studies, three possible schemes for the formation of N_2(C-B) are proposed. The first scheme starts with the formation of N_4^+ from the associative combination reaction reported as Reaction 39 in this work. The N_4^+ molecule quickly dissociates into N_2(C) and N_2, reported as Reaction 37 and 40 in this work. This scheme is supported by Ref [63,67,68]. Second is the collision-assisted reaction that crosses nitrogen systems. It involves the formation of a single excited state of $N_2 \rightarrow N_2^*$ followed by an electron collision to produce N_2(C) [69–71]. Finally, the third mechanism relies on direct excitation of $N_2(X) \rightarrow N_2(C)$ via direct electron impact, reported as Reaction 10 and supported by Refs [66,72–74]. An experimentally observed increase in the relative population of N_2(C) at a delay of 2 ns could indicate competing formation reactions where one becomes dominant over the others at later times in the post-discharge. A proposed reaction that could fit this description is the energy pooling reaction of $N_2(A^3 \sum_u^+)$, reported as Reaction 45 in this work and supported by Ref [77]. Clearly, there is a lack of literary consensus on the formation mechanism for the dominant species in the emission spectra of femtosecond laser-induced filaments. Given this, a chemical kinetics sensitivity analysis for all the competing mechanisms is presented in the next section.

4.6.3 $N_2(C)$ Sensitivity Analysis in fs-LASER Plasmas

The sensitivity analysis performed after the simulation was complete allows the determination of the formation and loss mechanisms for N_2(C) in our model. The results show that N_2(C) is initially populated via direct electron-impact excitation up from N_2(X) and is shown in the orange curve in Figure 39. In the early stages of the simulation, whilst the direct electron excitation is occurring, a parallel reaction is taking place that soon takes over as the dominant

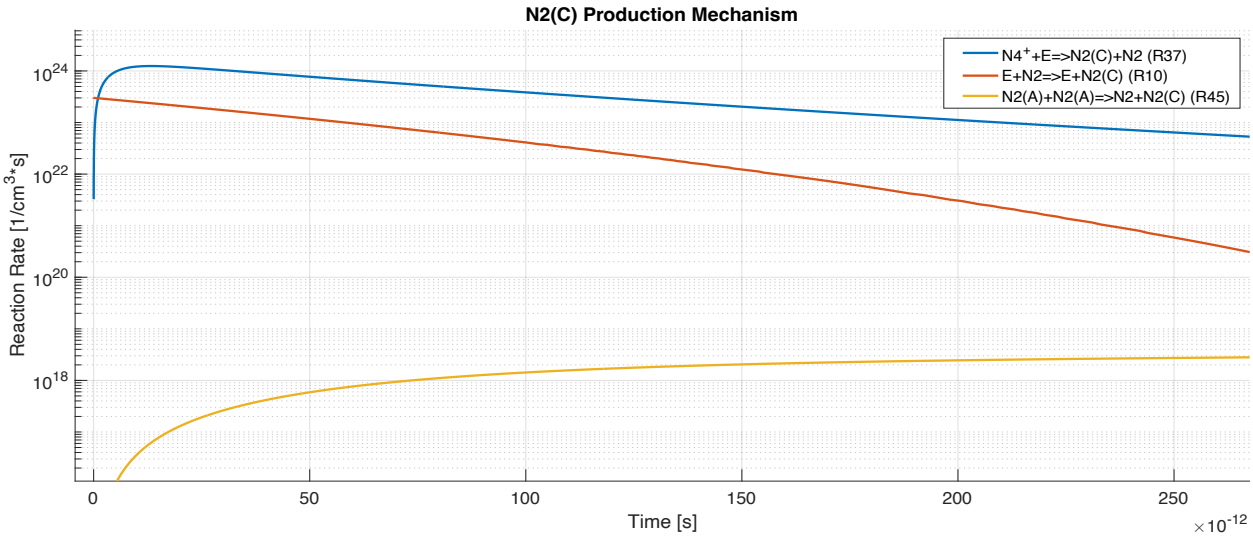

Figure 39. Temporal evolution of $N_2(C)$ formation mechanisms. The orange curve represents direct electron-impact excitation from the ground state, dominating in the initial picoseconds. The blue curve corresponds to N_4^+ dissociative recombination, which becomes the primary mechanism after N_4^+ reaches a critical threshold. The yellow curve represents the $N_2(A)$ pooling reaction. The reaction number for each process is reported in the legend c.f. Tables 1-3.

formation mechanism for $N_2(C)$. The associative combination of N_2^+ and N_2 to form N_4^+ as described in Reaction 39 generates large volumes of N_4^+. This unstable molecule dissociates into $N_2(C)$ as described in Reaction 37 and shown in blue in Figure 39. The proposed pooling reaction of $N_2(A)$ is also shown in the figure but does not provide a significant impact on the $N_2(C)$ population until 2 ns (the figure has a maximum time of 0.25 ns plotted). At this point, $N_2(A)$ pooling does become the dominant formation mechanism for $N_2(C)$, but the plasma emission from $N_2(C\text{-}B)$ has ceased due to the $N_2(C)$ species density falling beneath detection limits.

While formation is important, equally so is the destruction mechanisms for $N_2(C)$. The results shown that $N_2(C)$ is predominately quenched by O_2, then to a smaller order of magnitude N_2. The quenching rates, which were treated as inputs to our simulation, for N_2 and O_2 are about 10^{-11} cm^3/s and 2.7×10^{-10} cm^3/s respectively [78]. The deexcitation of $N_2(C\text{-}B)$ serves as a destruction mechanism, however on an order of magnitude lower still than the N_2 quenching reaction as shown in Figure 40.

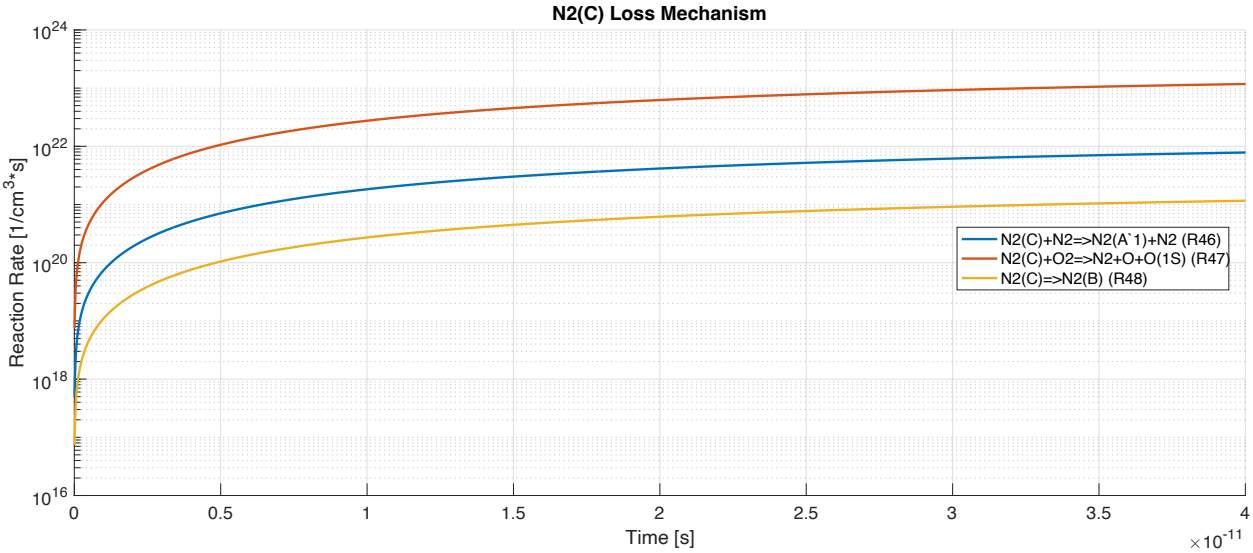

Figure 40. Temporal evolution of $N_2(C)$ loss mechanisms. The orange curve represents quenching by O_2, the blue curve corresponds to quenching by N_2, and the yellow curve illustrates the loss of $N_2(C)$ due to the $N_2(C\text{-}B)$ radiative transition. O_2 quenching dominates initially, while the $N_2(C\text{-}B)$ transition becomes a significant pathway later, aligning with experimental spectra observations.

The simulation also reports the time-evolved species density of all molecules and excited states captured in the model, and the ones involved in the reaction pathway for $N_2(C)$ are shown in Figure 41. Several distinct trends arise which support the formation and loss mechanism reported above. The density of $N_2(C)$ reaches a maximum at 0.25 ns into the simulation and then has a rapid decline, falling five orders of magnitude by 5 ns. Likewise, N_4^+ is formed in the initial picoseconds after the pulse, but decays at a faster rate than that of $N_2(C)$. This follows the logic of the proposed mechanism involving N_4^+ associative/dissociative combination, Reactions 37 & 39. Also shown on the plot is $N_2(A)$, responsible for the pooling reactions occurring at 2 ns. The density of this species remains unaffected by the $N_2(C)$ & N_4^+ beneath it. This also aligns with the formation mechanism, suggesting a nonsignificant contribution of $N_2(C)$ in the initial stages of the simulation.

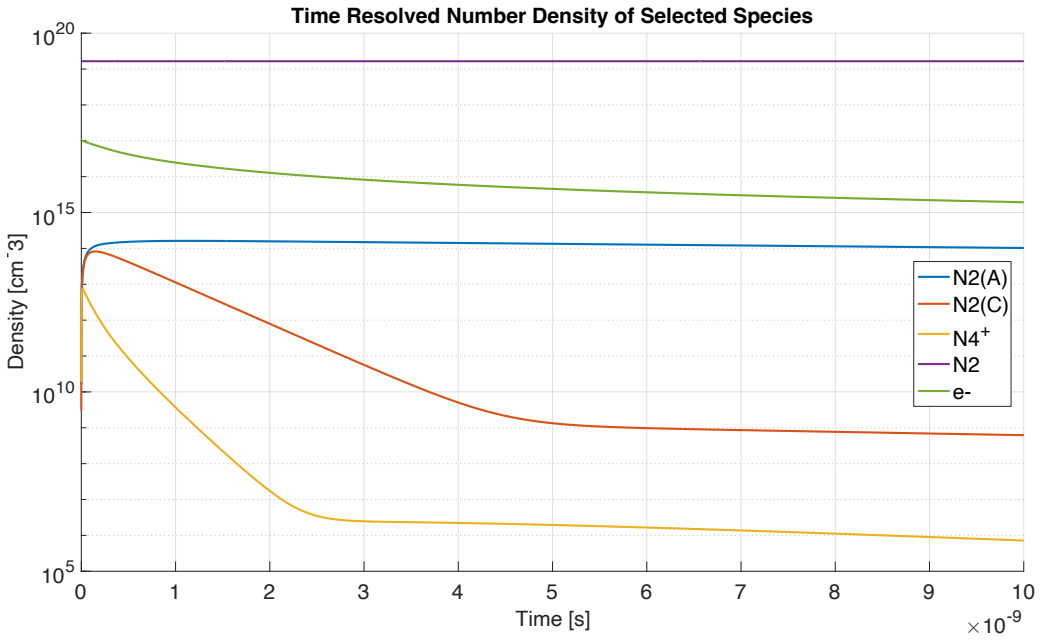

Figure 41. Temporal evolution of species number densities. $N_2(C)$ peaks early and decays rapidly, while N_4^+ declines more steeply over time.

4.6.4 $N_2(C)$ Experimental Data Comparison

To compare the experimental data against that of the model, we need to take the integral of the time-resolved spectra for $N_2(C)$, as shown in Figure 28 for the range of 365-390 nm. This range was chosen because only $N_2(C)$ emission is present here. The results of the numerical integration are normalized to the value at a delay of 0 ns. In Figure 42, we see good agreement between the fast decay of $N_2(C)$ between the experimental data and the model. However, the time at which that decay occurs is much sooner for the model than for the experiment. Several explanations can be found for this behavior. First is the time resolution of the camera being much coarser than that of the model. The camera operates on a minimum gate width of 2 ns, whilst the model has timesteps of 0.1 ns. Thus, in the case of the experimental data, we are only able to collect data on a timescale wherein most of the chemistry has already taken place. Secondly, due to experimental jitter from the equipment, a delay of 0 ns does not exactly occur at a true delay time of 0 ns. The camera has a reported jitter from triggering input to optical opening of 0.15 ns.

Finally, $N_2(C)$ has a radiative lifetime of about 39 ns. Given the previously reported quenching rates of $N_2(C)$ by N_2 and O_2, and assuming that the composition of air is in equilibrium at 500 K, the characteristic decay time of $N_2(C)$ due to first quenching and second spontaneous emission is about 1 ns. The spontaneous emission portion is what is responsible for the detectable plasma emission from the $N_2(C\text{-}B)$ transition.

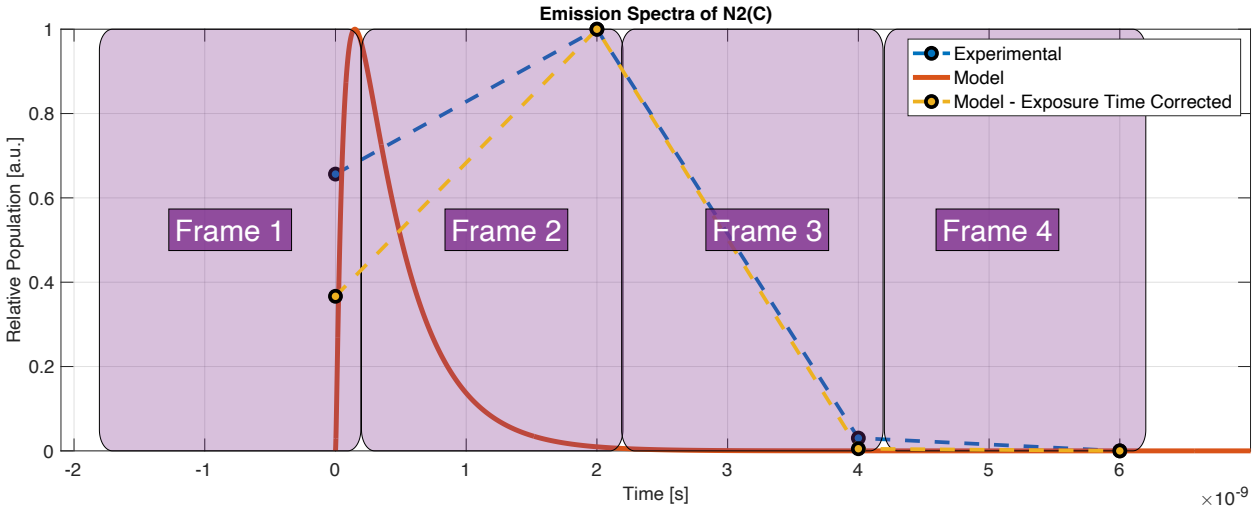

Figure 42. A comparison of experimental excited-state $N_2(C)$ emission data with modeled data. The experimental data was collected with frames of width 2 ns, shown by the purple squares. The cumulative sum of the model function is taken in the range of each of the frames and plotted against experimental data. All values are normalized to the maximum value in their respective datasets.

An effort was undertaken to mathematically model what the camera is capturing for the $N_2(C)$ species density as computed by the model. If one were to take the normalized cumulative sum Q of the values output by the model, you could find the timestep where the model equals that of the experimental data, $Q = 0.65$. We determined this value to be 0.195 ns. Changing our reference frame so that the model serves as the true delay of 0 ns, if we take the cumulative sum ending at the computed point where $Q = 0.65$, and beginning 2 ns into the past, we find that the first exposure of the camera lasts from $t = -1.806$ ns $\rightarrow 0.194$ ns. Now that our reference frames are aligned, we can continue to "take exposures" of the model data and report their cumulative sum. This is depicted as the purple squares in Figure 42. Therefore, according to our

model, the $N_2(C)$ emission is concurrent with the experimental data when one accounts for the larger timestep which the camera can capture by taking the cumulative sum of the modeled data in the frames for which the camera can expose.

CHAPTER 5: CONCLUSION

The objective of this thesis was to present the experimental results and zero-dimensional modeling of femtosecond filaments in air at atmospheric conditions to gain an understanding of the chemistry occurring therein. This objective was met first in Chapter 3 where we used optical emission spectroscopy to collect emissive data from the filament and using a synchronized iCMOS camera to temporally resolve the data. The data was then processed using the plasma radiative code Specair and through Boltzmann fitting, a determination of the main emissive species was made. Further, the gas temperature of the plasma was determined. In Chapter 4, the chemistry that occurred to generate the short-lived species observed was simulated by the ZDPlasKin solver using a model that replaced electron-impact reactions with an Arrhenius form. The Arrhenius form was generated using a custom-built code that integrated the cross-sectional data of the electron-impact reactions and the electron energy distribution function to solve for the reaction rate constant as a function of electron temperature. The conclusions that are drawn from Chapters 3 and 4 are summarized in the next section. The conclusion of this chapter presents the future research that needs to occur to further the work outlined here.

5.1 Summary

Chapter 3 presents an experimental testbed used to create and analyze a plasma filament generated by a femtosecond laser. The data revealed an extremely short-lived emission, with the plasma becoming undetectable after 8 ns post-discharge. The emission was dominated by the N_2 second positive system and the N_2^+ first negative system. These two species have been reported as the dominant emitters in other studies with similar conditions [61,63–66]. These two systems were determined via the global fitting Boltzmann analysis used by Specair. This fitting process allowed us to resolve the relative populations of each of the two dominant systems as a function

of time. This revealed a unique behavior in which the relative populations of both species increased at a delay of 2 ns relative to the time when the filament was first detectable by the camera. To try and understand the behavior, chemical kinetic pathways were considered for the formation of $N_2(C)$ and $N_2^+(B)$. For $N_2(C)$, one formation scheme was the formation via N_4^+ dissociation. N_4^+ forms from the associative combination reaction of N_2 and N_2^+ and is discussed in [63,67,68]. The second proposed mechanism was the result of an intersystem crossing assisted by an electron collision. In this method, a single state of N_2 gets excited to N_2^* which then interacts with an electron to become excited up to $N_2(C)$ as discussed in [69–71]. The third proposed mechanism was a direct electron excitation up from the ground state of $N_2(X)$ to $N_2(C)$ [66,72–74]. The fourth mechanism that could cause the delayed population increase is the $N_2(A)$ pooling reactions which form $N_2(C)$ [77].

For $N_2^+(B)$, the formation mechanism was equally unambiguous. It is thought that $N_2^+(B)$ could be formed via MPI and tunnel ionization of the inner-valence electrons attached to N_2 [61,67,70,75,76]. Equally valid is the assumption that $N_2^+(B)$ comes from direct electron excitation, similar to the third method proposed for $N_2(C)$, but from $N_2(X)$ [73] or $N_2^+(X)$ [68].

Further, the gas temperature was able to be inferred from the rotational temperature calculated due to the rotational-translational relaxation event occurring faster than the characteristic emission time for the two dominant species. It was found that the gas temperature was 500 ± 100 K.

Chapter 4 outlines a chemical kinetics model that was generated to be used by the zero-dimensional plasma kinetics solver ZDPlasKin in lieu of using BOLSIG+ to solve for the reaction rate constants of electron impact reactions. Arrhenius form equations were derived that integrated the cross-sectional data of electron-impact reactions with the electron energy

distribution function to generate discrete value for the reaction rate constant. The Arrhenius form of the reaction rate constants were used as inputs for the femtosecond laser-induced plasma simulations. These inputs were coupled with reaction rates proposed by Capitelli *et. al.* and Ivanov *et. al.* to complete the model [68,101].

These simulations produced time-dependent species densities as well as a sensitivity analysis, allowing the determination of the reaction pathways involved in generating those species. Particularly of interest was the formation and destruction mechanisms for $N_2(C)$ which dominated the emission of the data found in Chapter 3. The proposed mechanisms in Chapter 3 were integrated into the model, and it was found that $N_2(C)$ formation comes from an initial formation via direct electron excitation up from the ground state of $N_2(X)$ in the first 2 picoseconds after the pulse. Concurrently with this reaction, the formation of N_4^+ was occurring via associative combination of N_2 and N_2^+. The stability of this molecule is very low, so it dissociates into $N_2(C)$ and N_2 very quickly and becomes the dominant formation mechanism for the $N_2(C)$ species lasting into the first nanoseconds. $N_2(C)$ is destroyed by quenching via O_2 primarily, N_2 secondarily, and deexcited down to $N_2(B)$ ternately. It is this tertiary destruction method that provides the plasma emission detectable by our hardware. The time-resolved species density of $N_2(C)$ along with other molecules relevant to its reaction pathway were plotted, and the density of each species matched the logic behind the mechanisms determined. The $N_2(C)$ species density was also compared to the experimental work done. When the camera exposure was simulated as the cumulative sum of the density of the $N_2(C)$ population as a function of time, it was found that the model agrees well with the experimental data captured.

5.2 Future Work

The future work needed to advance what was found in this thesis will involve both experimental and modeling improvements. Improvements to the modeling work will involve improving the current mechanism to include the formation of $N_2^+(B)$. Whilst we have shown experimentally that $N_2^+(B)$ exists within the plasma on the same timescales as $N_2(C)$, the modeling of $N_2^+(B)$ requires the inclusion of a detailed model of $N_2(X)$ with vibrational levels greater than five, which is currently lacking in our model. Further, we assumed a Maxwellian distribution in order to calculate our EEDF generally for all reactions. The formation mechanisms which cause the filament to form involve rapid energy deposition and could lead to non-thermal equilibrium plasmas. This comes from the low electron density in the plasma and the dominant ionization mechanisms being multiphoton ionization and electron tunneling. Because of this, the EEDF should be measured directly or estimated numerically using a non-Maxwellian method.

Experimentally, others will need to use laser scattering methods to quantify the gas temperature of the filament to reinforce the determination made through Boltzmann analysis. One method that could work for this is Rayleigh scattering. Rayleigh scattering could also provide insights into the electron density in the filament, while Thomson scattering could quantify the electron temperature. Both of these methods provide a non-intrusive way to optically diagnose the properties of the filament. Through careful experimental procedures, it is possible to use Rayleigh scattering to determine densities [10]. Incoherent laser Thomson scattering (LTS) can be employed into our system with a Nd:YAG laser at 532 nm transverse to the filament. Work has already been done by others in our group for the LTS study of electron properties of a laser-induced plasma from a single pulse of an Nd:YAG at 1064 nm, 10 ns, and 25 mJ. The results of this illustrative study were able to determine the electron density and

temperatures by fitting a synthetic spectrum to the experimental results obtained from LTS using a Salpeter form-factor approximation [108–110]. Adding time resolution to those measurements was also possible by implementing an ICCD camera system. It has been demonstrated in the literature that the spatial resolution of such plasmas is also possible within ~100 μm, radially and axially [111].

5.3 Concluding Thoughts

This thesis comes at a moment in time when the focus and attention on femtosecond filaments could lead to their utilization in industry. I feel honored to be able to contribute in a small way to gaining an understanding of the chemical kinetics that occur with these filaments and to be able to participate in research in a field that is ripe with opportunities to improve combustion, aerospace, and laser diagnostic fields. I hope that the contributions that I have made with the work I have presented here will be found useful and that it will help others to continue to push forward and advance our knowledge of the universe around us.

REFERENCES

[1] Graham-Rowe D, Won R. Lasers for engine ignition. Nature Photonics 2008;2. https://doi.org/10.1038/nphoton.2008.161.

[2] Ju Y, Sun W. Plasma assisted combustion: Dynamics and chemistry. Progress in Energy and Combustion Science 2015;48:21–83. https://doi.org/10.1016/j.pecs.2014.12.002.

[3] Brieschenk S, O'Byrne S, Kleine H. Laser-induced plasma ignition studies in a model scramjet engine. Combustion and Flame 2013;160:145–8. https://doi.org/10.1016/j.combustflame.2012.08.011.

[4] O'Byrne S, Doolan M, Olsen SR, Houwing AFP. Analysis of transient thermal choking processes in a model scramjet engine. Journal of Propulsion and Power 2000;16:808–14. https://doi.org/10.2514/2.5645.

[5] Hooshyar U, Dumitrachep C. Computational Modeling of Femtosecond-Initiated Continuous Optical Discharge in Air. n.d.

[6] Brieschenk S, Kleine H, O'Byrne S. Laser ignition of hypersonic air-hydrogen flow. Shock Waves 2013;23:439–52. https://doi.org/10.1007/s00193-013-0447-6.

[7] Ronney PD. Laser versus conventional ignition of flames. Optical Engineering 1994:510–21.

[8] Dumitrache C, Azer A:, Yalin Co-Advisor P, Marchese AJ, Gao X, Orden AV, et al. NOVEL LASER IGNITION TECHNIQUE USING DUAL-PULSE PRE-IONIZATIO. Colorado State University, 2017.

[9] Shneider MN, Zheltikov AM, Miles RB. Tailoring the air plasma with a double laser pulse. Physics of Plasmas 2011;18. https://doi.org/10.1063/1.3601764.

[10] Dumitrache C, Limbach CM, Yalin AP. Threshold characteristics of ultraviolet and near infrared nanosecond laser induced plasmas. Physics of Plasmas 2016;23. https://doi.org/10.1063/1.4963248.

[11] Blanchard VP, Wilson S, Dumitrache C, Yalin AP. Characterization of a Femtosecond Filament in Air by Optical Emission Spectroscopy. AIAA Aviation Forum and ASCEND, 2024, American Institute of Aeronautics and Astronautics Inc, AIAA; 2024. https://doi.org/10.2514/6.2024-3724.

[12] Chin SL. Femtosecond Laser Filamentation. New York: Springer New York, NY; 2010.

[13] Couairon A, Mysyrowicz A. Femtosecond filamentation in transparent media. Physics Reports 2007;441:47–189. https://doi.org/10.1016/j.physrep.2006.12.005.

[14] Alshershby M, Hao Z, Camino A, Lin J. Modeling a femtosecond filament array waveguide for guiding pulsed infrared laser radiation. Optics Communications 2013;296:87–94. https://doi.org/10.1016/j.optcom.2012.12.067.

[15] Chin SL, Wang T-J, Marceau C, Wu J, Liu JS, Kosareva O, et al. Advances in intense femtosecond laser filamentation in air. Laser Physics 2012;22:1–53. https://doi.org/10.1134/s1054660x11190054.

[16] Raizer Y P. Gas Discharge Physics. Springer Berlin; 1991.

[17] Adelgren R, Elliot G, Knight D, Zheltovodov A, Beutner T. Energy deposition in supersonic flows. 39th Aerospace Sciences Meeting and Exhibit, Reston, Virigina: American Institute of Aeronautics and Astronautics; 2001. https://doi.org/10.2514/6.2001-885.

[18] Paschotta R. Nonlinear Index - an encyclopedia article. RP Photonics Encyclopedia, RP Photonics AG; 2006. https://doi.org/10.61835/ks8.

[19] Marburger JH. SELF-FOCUSING: THEORY. vol. 4. Pergamon Press; 1975.

[20] Augst S, Meyerhofer DD, Strickland D, Chint SL. Laser ionization of noble gases by Coulomb-barrier suppression. Journal of the Optical Society of America B 1991;8:858. https://doi.org/10.1364/josab.8.000858.

[21] Feit MD, Fleck JA. Effect of refraction on spot-size dependence of laser-induced breakdown. Applied Physics Letters 1974;24:169–72. https://doi.org/10.1063/1.1655139.

[22] Kasparian J, Sauerbrey R, Chin SL. The critical laser intensity of self-guided light filaments in air. Applied Physics B: Lasers and Optics 2000;71:877–9. https://doi.org/10.1007/s003400000463.

[23] Danehy PM, Bathel BF, Johansen CT, Winter M, O'byrne S, Cutler AD. Molecular-Based Optical Diagnostics for Hypersonic Nonequilibrium Flows. 2015.

[24] Rao A. Rapid Analysis of Plutonium Surrogate Material via Hand-Held Laser-Induced Breakdown Spectroscopy Laser-Induced Breakdown Spectroscopy n.d. https://doi.org/10.13140/RG.2.2.18732.74888.

[25] Spectral Fit SAS. Specair 2012.

[26] Laux CO, Spence TG, Kruger CH, Zare RN. Optical diagnostics of atmospheric pressure air plasmas. vol. 12. 2003.

[27] Pancheshnyi S, Eismann B, Hagelaar GJM, Pitchford LC. Computer code ZDPlasKin 2008.

[28] Hagelaar G. BOLSIG+ n.d.

[29] Luque A. QTPlasKin n.d.

[30] Hagelaar GJM, Pitchford LC. Solving the Boltzmann equation to obtain electron transport coefficients and rate coefficients for fluid models. Plasma Sources Science and Technology 2005;14:722–33. https://doi.org/10.1088/0963-0252/14/4/011.

[31] LAPLACE database n.d. www.lxcat.net (accessed November 15, 2024).

[32] Carbone E, Graef W, Hagelaar G, Boer D, Hopkins MM, Stephens JC, et al. Data needs for modeling low-temperature non-equilibrium plasmas: The LXCat project, history, perspectives and a tutorial. Atoms 2021;9:1–40. https://doi.org/10.3390/atoms9010016.

[33] Pitchford LC, Alves LL, Bartschat K, Biagi SF, Bordage MC, Bray I, et al. LXCat: an Open-Access, Web-Based Platform for Data Needed for Modeling Low Temperature Plasmas. Plasma Processes and Polymers 2017;14. https://doi.org/10.1002/ppap.201600098.

[34] Pancheshnyi S, Biagi S, Bordage MC, Hagelaar GJM, Morgan WL, Phelps AV, et al. The LXCat project: Electron scattering cross sections and swarm parameters for low temperature plasma modeling. Chemical Physics 2012;398:148–53. https://doi.org/10.1016/j.chemphys.2011.04.020.

[35] Bergé L, Skupin S, Nuter R, Kasparian J, Wolf J-P. Ultrashort filaments of light in weakly ionized, optically transparent media. Reports on Progress in Physics 2007;70:1633. https://doi.org/10.1088/0034-4885/70/10/R03.

[36] Chin SL, Hosseini SA, Liu W, Luo Q, Théberge F, Aközbek N, et al. The propagation of powerful femtosecond laser pulses in opticalmedia: physics, applications, and new challenges. Canadian Journal of Physics 2005;83:863–905. https://doi.org/10.1139/p05-048.

[37] Kasparian J, Wolf J-P. Physics and applications of atmospheric nonlinear optics and filamentation. Optics Express 2008;16:466–93. https://doi.org/10.1364/OE.16.000466.

[38] Sprangle P, Peñano JR, Hafizi B. Propagation of intense short laser pulses in the atmosphere. Phys Rev E 2002;66:046418. https://doi.org/10.1103/PhysRevE.66.046418.

[39] Vidal F, Comtois D, Chien C-Y, Desparois A, Fontaine BL, Johnston TW, et al. Modeling the Triggering of Streamers in Air by Ultrashort Laser Pulses. vol. 28. 2000.

[40] Théberge F, Daigle JF, Kieffer JC, Vidal F, Châteauneuf M. Laser-guided energetic discharges over large air gaps by electric-field enhanced plasma filaments. Scientific Reports 2017;7. https://doi.org/10.1038/srep40063.

[41] Gao Q, Zhu Z, Li B, Han L, Li Z. Spatiotemporally resolved spectra of gaseous discharge between electrodes triggered by femtosecond laser filamentation. Applied Physics B 2022;128:184. https://doi.org/10.1007/s00340-022-07907-7.

[42] Houard A, Walch P, Produit T, Moreno V, Mahieu B, Sunjerga A, et al. Laser-guided lightning. Nature Photonics 2023;17:231–5. https://doi.org/10.1038/s41566-022-01139-z.

[43] Wolf JP. Short-pulse lasers for weather control. Reports on Progress in Physics 2018;81. https://doi.org/10.1088/1361-6633/aa8488.

[44] Elias P-Q, Severac N, Luyssen J-M, Tobeli J-P, Bur R, André Y-B, et al. Femtosecond Laser Energy deposition in a M=3 Supersonic Flow: Parametric Study n.d. https://doi.org/10.13009/EUCASS2019-681.

[45] Ding P, Oliva E, Houard A, Mysyrowicz A, Liu Y. Lasing dynamics of neutral nitrogen molecules in femtosecond filaments. Physical Review A 2016;94:43824. https://doi.org/10.1103/PhysRevA.94.043824.

[46] Kartashov D, Ališauskas S, Andriukaitis G, Pugžlys A, Shneider M, Zheltikov A, et al. Free-space nitrogen gas laser driven by a femtosecond filament. Physical Review A 2012;86:33831. https://doi.org/10.1103/PhysRevA.86.033831.

[47] D'Amico C, Houard A, Franco M, Prade B, Mysyrowicz A, Couairon A, et al. Conical Forward THz Emission from Femtosecond-Laser-Beam Filamentation in Air. Physical Review Letters 2007;98:235002. https://doi.org/10.1103/PhysRevLett.98.235002.

[48] Zhang D, Gao Q, Li B, Zhu Z, Li Z. Instantaneous one-dimensional equivalence ratio measurements in methane/air mixtures using femtosecond laser-induced plasma spectroscopy. Optics Express 2019;27:2159. https://doi.org/10.1364/oe.27.002159.

[49] Zang H, Li H, Zhang W, Fu Y, Chen S, Xu H, et al. Robust and ultralow-energy-threshold ignition of a lean mixture by an ultrashort-pulsed laser in the filamentation regime. Light: Science and Applications 2021;10. https://doi.org/10.1038/s41377-021-00496-8.

[50] Zhang W, Zang H, Wang S, Chen J, Li H, Xu H, et al. Non-resonant photochemical ignition of lean methane/air mixtures by femtosecond laser filamentation. Combustion and Flame 2024;266. https://doi.org/10.1016/j.combustflame.2024.113542.

[51] Wille H, Rodriguez M, Kasparian J, Mondelain D, Yu J, Mysyrowicz A, et al. Teramobile: A mobile femtosecond-terawatt laser and detection system. Eur Phys J AP 2002;20:183–90.

[52] Méjean G, Ackermann R, Kasparian J, Salmon E, Yu J, Wolf J-P, et al. Improved laser triggering and guiding of meqavolt discharges with dual fs-ns pulses. Applied Physics Letters 2006;88:021101. https://doi.org/10.1063/1.2162430.

[53] Henis Z, Milikh G, Papadopoulos K, Zigler A. Generation of controlled radiation sources in the atmosphere using a dual femtosecond /nanosecond laser pulse. Journal of Applied Physics 2008;103:103111. https://doi.org/10.1063/1.2927457.

[54] Zhou B, Akturk S, Prade B, André Y-B, Houard A, Liu Y, et al. Revival of femtosecond laser plasma filaments in air by a nanosecond laser. Optics Express 2009;17:11450. https://doi.org/10.1364/OE.17.011450.

[55] Papeer J, Botton M, Gordon D, Sprangle P, Zigler A, Henis Z. Erratum: Extended lifetime of high density plasma filament generated by a dual femto-nanosecond laser pulse (New

Journal of Physics (2014) 16 (123046)). New Journal of Physics 2015;17. https://doi.org/10.1088/1367-2630/17/8/089501.

[56] Papeer J, Botton M, Gordon D, Sprangle P, Fibich G, Herzig Sheinfux H, et al. Multi variable control of filamentation of femtosecond laser pulses propagating in air. Journal of Physics B: Atomic, Molecular and Optical Physics 2015;48. https://doi.org/10.1088/0953-4075/48/9/094005.

[57] Li B, Li X, Zhu Z, Gao Q. Nanosecond laser-induced breakdown assisted by femtosecond laser pre-ionization in air: the effect on spatial resolution and continuous radiation. Eur Phys J Appl Phys 2020;92.

[58] Bak J, Pokharel S, Hadden H, Naidu A, Ruggles KT, Tropina A, et al. Laser intensity shaping: hydrodynamic effects and energy coupling in dual pulse laser energy deposition. AIAA SCITECH 2024 Forum, American Institute of Aeronautics and Astronautics; 2024. https://doi.org/10.2514/6.2024-2241.

[59] Solstice Ace User's Manual One-Box Ultrafast Amplifier System. 2016.

[60] pco.dicam C1 UHS Data Sheet n.d.

[61] Talebpour A, Petit S, Chin SL. Re-focusing during the propagation of a focused femtosecond Ti:Sapphire laser pulse in air. vol. 171. 1999.

[62] Talebpour A, Abdel-Fattah M, Bandrauk A, Chin SL. Spectroscopy of the gases interacting with intense femtosecond laser pulses. Laser Physics 2001;11:68–76.

[63] Xu HL, Azarm A, Bernhardt J, Kamali Y, Chin SL. The mechanism of nitrogen fluorescence inside a femtosecond laser filament in air. Chemical Physics 2009;360:171–5. https://doi.org/10.1016/j.chemphys.2009.05.001.

[64] Ilyin AA, Golik SS, Shmirko KA. Absorption and emission characteristics of femtosecond laser plasma filaments in the air. Spectrochimica Acta Part B: Atomic Spectroscopy 2015;112:16–22. https://doi.org/10.1016/j.sab.2015.08.002.

[65] Finney LA, Skrodzki PJ, Burger M, Xiao X, Nees J, Jovanovic I. Optical emission from ultrafast laser filament-produced air plasmas in the multiple filament regime. Optics Express 2018;26:29110. https://doi.org/10.1364/oe.26.029110.

[66] Danylo R, Zhang X, Fan Z, Zhou D, Lu Q, Zhou B, et al. Formation Dynamics of Excited Neutral Nitrogen Molecules inside Femtosecond Laser Filaments. Physical Review Letters 2019;123. https://doi.org/10.1103/PhysRevLett.123.243203.

[67] Wang P, Xu S, Li D, Yang H, Jiang H, Gong Q, et al. Spectroscopic study of laser-induced tunneling ionization of nitrogen molecules. Physical Review A - Atomic, Molecular, and Optical Physics 2014;90. https://doi.org/10.1103/PhysRevA.90.033407.

[68] Ivanov NG, Losev VF, Prokop'ev VE, Sitnik KA, Zyatikov IA. High time-resolved spectroscopy of filament plasma in air. Optics Communications 2019;431:120–5. https://doi.org/10.1016/j.optcom.2018.09.007.

[69] Arnold BR, Roberson SD, Pellegrino PM. Excited state dynamics of nitrogen reactive intermediates at the threshold of laser induced filamentation. Chemical Physics 2012;405:9–15. https://doi.org/10.1016/j.chemphys.2012.05.019.

[70] Li S, Wang Y, Zhang Y, Liang C, Yu M, Liu Y, et al. Nitrogen fluorescence emission induced by femtosecond vortex beams in air. Physica Scripta 2023;98. https://doi.org/10.1088/1402-4896/acc90e.

[71] Li S, Sui L, Chen A, Jiang Y, Liu D, Shi Z, et al. Angular distribution of plasma luminescence emission during filamentation in air. Physics of Plasmas 2016;23. https://doi.org/10.1063/1.4940941.

[72] Yao J, Xie H, Zeng B, Chu W, Li G, Ni J, et al. Gain dynamics of a free-space nitrogen laser pumped by circularly polarized femtosecond laser pulses. Optics Express 2014;22:19005. https://doi.org/10.1364/oe.22.019005.

[73] Mitryukovskiy S, Liu Y, Ding P, Houard A, Couairon A, Mysyrowicz A. Plasma luminescence from femtosecond filaments in air: Evidence for impact excitation with circularly polarized light pulses. Physical Review Letters 2015;114. https://doi.org/10.1103/PhysRevLett.114.063003.

[74] Zheng W, Miao Z, Dai C, Wang Y, Liu Y, Gong Q, et al. Formation Mechanism of Excited Neutral Nitrogen Molecules Pumped by Intense Femtosecond Laser Pulses. Journal of Physical Chemistry Letters 2020;11:7702–8. https://doi.org/10.1021/acs.jpclett.0c02337.

[75] Becker A, Bandrauk AD, Chin SL. S-matrix analysis of non-resonant multiphoton ionisation of inner-valence electrons of the nitrogen molecule. vol. 343. 2001.

[76] Wang P, Wu C, Lei M, Dai B, Yang H, Jiang H, et al. Population dynamics of molecular nitrogen initiated by intense femtosecond laser pulses. Physical Review A - Atomic, Molecular, and Optical Physics 2015;92. https://doi.org/10.1103/PhysRevA.92.063412.

[77] Piper LG. State-to-state N2(A 3Σu+) energy-pooling reactions. I. The formation of N2(C 3Πu) and the Herman infrared system. The Journal of Chemical Physics 1988;88:231–9. https://doi.org/10.1063/1.454649.

[78] Valk F, Aints M, Paris P, Plank T, Maksimov J, Tamm A. Measurement of collisional quenching rate of nitrogen states N 2(C3Πu, υ = 0) and N2+(B2Σ+g, υ = 0). Journal of Physics D: Applied Physics 2010;43. https://doi.org/10.1088/0022-3727/43/38/385202.

[79] Chen S, Liu X-L, Lu X, Ma J, Wang J, Zhu B, et al. Temporal evolution of femtosecond laser filament detected via magnetic field around plasma current. Optics Express 2017;25:32514. https://doi.org/10.1364/oe.25.032514.

[80] Popov NA. Fast gas heating in a nitrogen-oxygen discharge plasma: I. Kinetic mechanism. Journal of Physics D: Applied Physics 2011;44. https://doi.org/10.1088/0022-3727/44/28/285201.

[81] Rusterholtz D, Pai D, Stancu G, Lacoste D, Laux C. Ultrafast Heating in Nanosecond Discharges in Atmospheric Pressure Air. 50th AIAA Aerospace Sciences Meeting including the New Horizons Forum and Aerospace Exposition, American Institute of Aeronautics and Astronautics; 2012. https://doi.org/10.2514/6.2012-509.

[82] Phelps AV, Pitchford LC. Anisotropic scattering of electrons by N 2 and its effect on electron transport. Phys Rev A 1985;31:2932–49. https://doi.org/10.1103/PhysRevA.31.2932.

[83] Puech V, Torchin L. Collision cross sections and electron swarm parameters in argon. J Phys D: Appl Phys 1986;19:2309–23. https://doi.org/10.1088/0022-3727/19/12/011.

[84] Alves LL. The IST-LISBON database on LXCat. J Phys: Conf Ser 2014;565:012007. https://doi.org/10.1088/1742-6596/565/1/012007.

[85] Morgan WL. A critical evaluation of low-energy electron impact cross sections for plasma processing modeling. I: Cl2, F2, and HCl. Plasma Chem Plasma Process 1992;12:449–76. https://doi.org/10.1007/BF01447254.

[86] Rogoff GL, Kramer JM, Piejak RB. A model for the bulk plasma in an RF chlorine discharge. IEEE Trans Plasma Sci n.d.;PS-14:103–11.

[87] Crompton RW, editor. Gaseous electronics and its applications. Tokyo : Dordrecht ; Boston: KTK Scientific Publishers ; Kluwer Academic Publishers; 1991.

[88] Pitchford LC, Boeuf J. SIGLO n.d.

[89] Bacri J, Medani A. Electron diatomic molecule weighted total cross section calculation. Physica B+C 1982;112:101–18. https://doi.org/10.1016/0378-4363(82)90136-X.

[90] Tennyson J, Brown D. Quantemol n.d.

[91] Hayashi M. Electron Collision Cross-Sections for Molecules Determined from Beam and Swarm Data. In: Pitchford LC, McKoy BV, Chutjian A, Trajrnar S, editors. Swarm Studies and Inelastic Electron-Molecule Collisions, New York, NY: Springer New York; 1987, p. 167–87. https://doi.org/10.1007/978-1-4612-4662-6_33.

[92] Abreu VJ, Yee JH, Solomon SC, Dalgarno A. The quenching rate of O(1D) by O(3P). Planetary and Space Science 1986;34:1143–5. https://doi.org/10.1016/0032-0633(86)90026-7.

[93] Felder W, Young RA. Quenching of O(1 *S*) by O(3 *P*). The Journal of Chemical Physics 1972;56:6028–30. https://doi.org/10.1063/1.1677150.

[94] Sadeghi N, Setser DW, Francis A, Czarnetzki U, Döbele HF. Quenching rate constants for reactions of Ar(4p′[1/2], 4p[1/2], 4p[3/2]2, and 4p[5/2]2) atoms with 22 reagent gases. The Journal of Chemical Physics 2001;115:3144–54. https://doi.org/10.1063/1.1388037.

[95] Niemi K, Gathen VSD, Döbele HF. Absolute atomic oxygen density measurements by two-photon absorption laser-induced fluorescence spectroscopy in an RF-excited

atmospheric pressure plasma jet. Plasma Sources Sci Technol 2005;14:375–86. https://doi.org/10.1088/0963-0252/14/2/021.

[96] Bittner J, Kohse-höinghaus K, Meier U, Just Th. Quenching of two-photon-excited H(3s, 3d) and O(3p 3P2,1,0) atoms by rare gases and small molecules. Chemical Physics Letters 1988;143:571–6. https://doi.org/10.1016/0009-2614(88)87068-4.

[97] Macko P, Veis P, Cernogora G. Study of oxygen atom recombination on a Pyrex surface at different wall temperatures by means of time-resolved actinometry in a double pulse discharge technique. Plasma Sources Sci Technol 2004;13:251–62. https://doi.org/10.1088/0963-0252/13/2/009.

[98] Kossyi IA, Kostinsky AY, Matveyev AA, Silakov VP. Kinetic scheme of the non-equilibrium discharge in nitrogen-oxygen mixtures. Plasma Sources Sci Technol 1992;1:207–20. https://doi.org/10.1088/0963-0252/1/3/011.

[99] Guerra V, Sá PA, Loureiro J. Kinetic modeling of low-pressure nitrogen discharges and post-discharges. Eur Phys J Appl Phys 2004;28:125–52. https://doi.org/10.1051/epjap:2004188.

[100] Gordiets BF, Ferreira CM, Guerra VL, Loureiro JMAH, Nahorny J, Pagnon D, et al. Kinetic model of a low-pressure N/sub 2/-O/sub 2/ flowing glow discharge. IEEE Trans Plasma Sci 1995;23:750–68. https://doi.org/10.1109/27.467998.

[101] Capitelli M, Ferreira CM, Gordiets BF, Osipov AI. Plasma Kinetics in Atmospheric Gases. vol. 31. Berlin, Heidelberg: Springer Berlin Heidelberg; 2000. https://doi.org/10.1007/978-3-662-04158-1.

[102] Martin F, Mawassi R, Vidal F, Gallimberti I, Comtois D, Pépin H, et al. Spectroscopic Study of Ultrashort Pulse Laser-Breakdown Plasmas in Air. Appl Spectrosc 2002;56:1444–52. https://doi.org/10.1366/00037020260377742.

[103] Mitchell KB. Fluorescence Efficiencies and Collisional Deactivation Rates for N2 and N2+ Bands Excited by Soft X Rays. The Journal of Chemical Physics 1970;53:1795–802. https://doi.org/10.1063/1.1674257.

[104] Talebpour A, Yang J, Chin SL. Semi-empirical model for the rate of tunnel ionization of N2 and O2 molecule in an intense Ti:sapphire laser pulse. Optics Communications 1999;163:29–32. https://doi.org/10.1016/S0030-4018(99)00113-3.

[105] Mur VD, Popruzhenko SV, Popov VS. Energy and momentum spectra of photoelectrons under conditions of ionization by strong laser radiation (The case of elliptic polarization). J Exp Theor Phys 2001;92:777–88. https://doi.org/10.1134/1.1378169.

[106] Dumitrache C, Butte C, Yalin A. Resonant dual-pulse laser ignition technique based on oxygen REMPI pre-ionization. Scientific Reports 2020;10:19916. https://doi.org/10.1038/s41598-020-76968-5.

[107] El-Rabii H, Victorov SB, Yalin AP. Properties of an air plasma generated by ultraviolet nanosecond laser pulses. Journal of Physics D: Applied Physics 2009;42:075203. https://doi.org/10.1088/0022-3727/42/7/075203.

[108] Hutchinson IH. Principles of Plasma Diagnostics. Cambridge: Cambridge University Press; 2002. https://doi.org/10.1017/CBO9780511613630.

[109] Friss A. Cavity Enhanced Thomson Scattering For Plasma Diagnostics. 2020.

[110] Friss AJ, Yalin AP. Cavity-enhanced Thomson scattering measurements of electron density and temperature in a hollow cathode discharge. Optics Letters 2018;43:5343–6. https://doi.org/10.1364/OL.43.005343.

[111] Dzierzęga K, Mendys A, Pokrzywka B. What can we learn about laser-induced plasmas from Thomson scattering experiments. Spectrochimica Acta Part B: Atomic Spectroscopy 2014;98:76–86. https://doi.org/10.1016/J.SAB.2014.03.010.